On the Computational Statistics of Random Walks

in discrete, confined, multi-dimensional domains

by

███████████

Department of Engineering Mathematics
UNIVERSITY OF BRISTOL

A dissertation submitted to the University of Bristol in accordance with the requirements for award of the Master's degree of Engineering Mathematics in the Faculty of Engineering.

FRIDAY 8TH MAY, 2020

Supervisor: ███████████

Word count: 13,472.
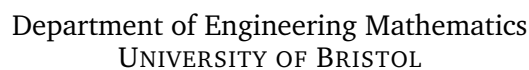
ABSTRACT

This paper attempts to elucidate the relationship between random walk algorithms and their descriptor statistics such as the first-passage time, cover time, and others. We include one chapter on the background of our problem and one chapter on some introductory principles. We dedicate the remainder to the research itself, divided into two partially standalone chapters. The first extends the concept of occupational probability through the Z-transform and presents numerical solutions to, and properties of, the first-passage time distribution. In this chapter we also separately investigate the enumeration of paths available to a random walker, wherein we build recurrence relations and show the structure and properties of the geometry that these relations imply. The second original chapter studies the typical behaviours observed in exhaustive search tasks, in which an entire domain must be visited, when performed under different walking conditions. A unique contribution we make to the literature is in our inclusion of a standstill probability. Its effects, additional to those of varying dimensionality, lattice size, and initial conditions, are found to be relevant everywhere and are reported throughout.

i

1

Since its inception in the Renaissance, classical probability theory has been extremely well-established and its practicalities realised worldwide. However, even before this, random walks – whose main tool of analysis is probability theory – were correctly identified and mathematically assessed. The earliest such example is from a letter sent by Blaise Pascal to Pierre de Fermat in 1656, where they discuss a rudimentary version of the famous gambler's ruin scenario. In this letter Pascal described a stochastic dice-based game in which points are added similarly to how a random walk's position evolves through time. It is then perhaps surprising that random walks of any kind only got their first mention by name in scientific literature at the turn of the 20th century.

The early days of research on random walks and other stochastic processes were largely application-oriented – not a contrast from the general state of mathematics at the time. Problems faced then were met with such a focus on praxis that often two or more works in analogous fields would have their similarities unnoticed for decades. One such case involves published works by Albert Einstein on Brownian motion [1905] and Karl Pearson on the time-evolution of random walker dispersion [1905]; both were published less than a year apart but Einstein was mostly concerned with calculating diffusion coefficients and Pearson with his own methodology. Although well-known now, the correspondence between random walks and particle diffusion went unnoticed until the 1960s when review papers began consolidating works from this era.

Still, progress in random walk theory has been tremendous and nowadays it enjoys sprawling applications, covering many contexts at many scales, as a result of co-operation between theoreticians and their practical counterparts. Twitter's *Who-To-Follow* service, which recommends users to other users, is wholly founded on random walk mechanics [Lin et al., 2013]. The path foraging animals follow when scavenging their territory is regarded as a random walk [Bénichou et al., 2011] for the purposes of studying habitats and the animals' dispersion within. Famously difficult to model in continuous time, diffusion-reaction systems can be accurately modelled by random lattice walks – the process by which proteins search and attach to certain genes is one example of this [Viswanathan et al., 2008].
Looking further afield, *biased* random walks – where one direction is preferred by the walker – have useful implementations in modelling chemotactic bacteria and diffusion dynamics [Flanders, 2019], and in decisions relating to advertisements on social media [Adal et al., 2010].

The term *random walk* (RW) is often used loosely to describe many different variants of the same underlying concept; stochastic, accumulative movement through a medium. In this paper *random walk* and related terms will exclusively refer to discrete-time processes on the D-dimensional integer lattice, denoted $\mathbb{Z}^D$, bound to some primitive hypercubic shape. The term *primitive* and its context is clarified in Chapter 2. Additionally, many papers on the topic investigate results for periodic boundaries (where crossing a boundary takes the walker to the opposite end of the lattice), absorbing boundaries (where the RW terminates on contact with an edge), or others. This research, however, is only concerned with the reflective case, where movement perpendicular to the lattice edge is reversed on contact.

Analysis of discrete-time RWs on Bravais lattices – of which the primitive cube is one – has the valuable advantage of avoiding the boundary value issues that appear in continuous systems. A researcher looking at the encounter times of two continuous walkers, for example, would have to either use the calculus-based idea of infinitesimals to look for overlap in the time either walker spends at a certain node, or sacrifice accuracy by looking for an encounter in an interval $[t, t+\delta t]$. In terms of spatial discreteness, difficulties arise where problems require small spatial quantities. For example, research on narrow escape theory by Holcman et al. [2018] calls for the calculation of the ratio between a neuron's somatic surface area and the absorbing area, which can be very difficult to compute without discretisation. With the advent of certain software this has been made somewhat easier and more accurate, though a new, similar issue has arisen in recent years. Most commonly encountered in robotics, gauging whether a given domain has been *covered* – i.e. whether the robot has searched everywhere – is unfeasible for continuous space. For these reasons, this research is concerned only with discrete space and discrete time.

The rest of this chapter will look at the in-depth body of work completed in the 20th century by A. M. Nemirovsky, G. H. Weiss, and other well-known researchers in the field of applied random walk theory. One problem with historic significance in the field is the problem of *coverage*. This refers to problems where an algorithm exhibits RW behaviour, with the main goal being to visit every node in the domain. Such problems were first researched in 1990, when introduced by Nemirovsky et al. [1990]. To date, one of the most notable results – discovered by this same paper – is that the time to visit the entire domain for $D = 1$ can be solved analytically through reduction to a first-visit problem. This is elucidated further in Section 1.1.

For $D > 1$, however, it was shown that the problem is irreducible to any known RW problem. This is due to the very different nature of the covering problem when $D > 1$. This stems from the property of 1D spaces to define their own unique path that joins any two sites, and the loss of this property for $D > 1$. In other words, there is a sole path that connects two given nodes on a 1D lattice but in 2D (and higher) there exist, in the infinite limit of the lattice size, infinitely many paths to connect two given nodes. Although an exact formulation for $D > 1$ cover times is beyond the scope of this paper, we conjecture their general dynamics by means of Monte Carlo simulations and provide affiliated statistics.

1.1   Literature Review

RW research has been ongoing since 1900, with the large majority of in-depth analyses being published after 1960. One of the earliest discussions mentioning RWs by name began with Karl Pearson in 1905, where he posited the drunkard's walk problem; if a drunk man, starting at the origin, takes a step of

one yard and turns "through any angle whatever" repetitively, how far would he get? This inspired a response from fellow mathematician Lord Rayleigh within just a week. Rayleigh did not formalise and solve the problem within a week, rather he related the question to a more general problem he solved decades earlier concerning the waves with stochastic phases. After some discourse, Pearson famously concluded:

> "the most probable place to find a drunken man who is at all capable of keeping on his feet is somewhere near his starting point!" [Ehrhardt, 2013]

This alludes to the now-common notion that random 2D lattice walks are *recurrent*, meaning that, given enough time, a random walker will return to its origin infinitely many times, even in an infinite domain. Nowadays we know that this specifically applies to symmetric RWs for $D \leqslant 2$:

> "A drunk man will find his way home, but a drunk bird may get lost forever." [Lugo, 2007]

Predating Pearson's conclusion by five years, Louis Bachelier applied the same mathematics to the world of finance in 1900 in his doctoral thesis. Albeit underappreciated for over 60 years, it eventually gained him status as a pioneer in the study of stochastic processes. His thesis, *La Théorie de la Spéculation* [1900], proposed the random walk model for the valuation of stock options, conjecturing that fluctuations in these prices are essentially random and cannot be beaten by a reasonable stock broker. Later, this idea would be extended to form the *efficient market hypothesis* and its corollary, the *random walk hypothesis*. The former applies Bachelier's groundwork to state that, because traders have near-instant access to pricing information, the stock market always values shares accurately, despite all traders not having access. The latter specifies that this manifests as an unpredictable RW and concludes rather strongly that, as a direct consequence, long-term risk-adjusted profit can only be had from insider trading. Both are in widespread use today (although the latter is usually interpreted less stringently) as the backbone of lead asset-pricing theories for much of the developed world.

Nemirovsky et al. [1990] were the first to pose the cover time problem, and their paper contributes to the literature both a power law and a logarithmic expression for the asymptotic cover time. Analytic coverage expressions, however, were found to only be solvable for the $D = 1$ problem as admitted by the authors; this is due to the challenges that higher-dimension irreducibility poses (as explained in the introductory text to this chapter). The 1D analytic coverage time expression was obtained by reduction to two *first-passage* problems. For a walker starting at node 1 (or N) they conjectured the form $N(N-1)$ for the time to reach node N (or 1) by means of Monte Carlo simulations. This was actually backed by an exact solution courtesy of Yokoi et al. [1990] who also reached the answer of $t_R = N(N-1)$, where t_R is the cover time, by method of generating functions. From there, the full solution simply required an extension of t_R such that the walker starts at arbitrary node s, travels to node 1 (or N) and only then traverses the lattice and finishes on node N (or 1). By the same generating function method, the cover time from s was found to be $t_R(s) = N(N-1) + (s-1)(N-s)$. Nemirovsky et al. also provide t_R for circular (periodic) 1D lattices as $t_R = \frac{1}{2}N(N-1)$, showing independence of s, as suspected; rigid lattices (reflective boundary conditions) do not enjoy the benefits of translational invariance that periodic lattices do.

The cover time problem was looked at again by Nemirovsky and Coutinho-Filho [1991], this time exploring the theory behind it more rigorously. By cascading infinite sums and using multiple generating functions, they arrive at the conclusion that the cover time problem cannot be solved easily for $D = 1$ for large N as "the algebra becomes quite involved" and their approach "appears hopeless". They conclude

that the problem therefore *requires* alternative formulation, as in Yokoi et al. [1990]. The second half of their research looks at a simplification of this where the walker is given *infinite range*; a RW with this property is no longer constrained to move a single step from its current location and can now jump to any other site on the lattice. A strong parallel is drawn between this infinite-range RW coverage question and the combinatorial question of filling N boxes with n balls at one ball per timestep, where the order of ball placement matters. This is the idea behind *mean field* approximations; reducing the problem to a minimalist form and using that as a starting point for its solution. Ultimately, they conjecture a function $w_N(n)$ for the mean field approximation of covering the lattice at timestep n, finding its first moment (i.e. the mean lattice covering time) in accordance with Monte Carlo data from Nemirovsky et al. [1990]. This work lays the groundwork for an exact formulation of $w_N(n)$, itself a stepping-stone to an analytic expression for the lattice cover time for $D > 1$.

Another paper of interest is by Chupeau et al. [2015]; *Cover Times of Random Searches*. The paper begins by reiterating the historic evasiveness of the cover time problem and provides a good explanation of context throughout. Chupeau et al. determine coverage times for a multitude of RW processes, and determine the distribution of the more general metric, *partial cover time*. This is denoted $\tau(M,N)$ and is the expected time to visit M of the N lattice sites for these processes. In deriving this, they first define $\theta(N-k,N) = \tau(k+1,N) - \tau(k,N)$. This equates to the mean time needed to visit a distinct site after k distinct visits. They then use results from two supporting papers to obtain a full distribution for θ in terms of the global mean first-passage time (MFPT), $\langle T \rangle$ – this is just the MFPT to reach a node averaged over all possible starting positions. The full distribution of θ is then just a special case of the partial coverage function and, after some rearrangement in the Laplace domain, the authors reach a computable distribution for this partial coverage distribution. As stated in Chupeau et al. [2015], partial coverage nowadays has wide-reaching uses in biochemistry, mainly involving the diffusion-reaction of two or more particles, and ecology and robotics, where the main concern is with territorial searches.

Despite the origins of RW research being sparked by very practical inspirations – e.g. the drunkard's walk problem and diffusivity calculations – the literature can be seen to have slowly detached from these roots, adopting abstract methods to solve abstract problems with salience on setting challenges rather than solving grounded problems. Of course this is not to be taken as a negative comment – after all, outside of economics (where RWs are more a descriptor model rather than a topic of research), large-scale relevant applications did not emerge until the end of the 20th century. As a result, recent papers (from the 21st century onwards) are remitting to the grounded, practical kind of problems that started this field.

Recent reviews that encapsulate this well include a paper by Xia et al. [2019], which outlines the varied applications of RWs found in the field of computer science alone, and by Galceran and Carreras [2013] which does the same for the open-ended task of coverage path planning in the field of robotics. Both showcase great achievements by the applied mathematics community in finding efficient, interdisciplinary improvements to solutions that, for a long time, were generally considered fine as is. Perhaps the pinnacle of this is in a paper referenced by Galceran and Carreras, on the possible implementation and optimisation of automated crop harvesters. Done by integrating their coverage path planning techniques (based on RW theory) and state-of-the-art computer vision, this is an application very few, if any, expected out of random walk theory, but that could have benefits felt across the globe.

DYNAMICS OF RANDOM WALKERS

The *isotropic* or *symmetric* random walk algorithm, as used in all simulations and analyses in this paper, is depicted in Figure 2.1. This walk has a probability $1 - p$ of staying in place – called its *standstill* probability – and a probability p of taking a step – called its *total* movement probability. Starting with the one-dimensional case, each non-standstill movement option – *left* or *right* – has a constant probability $\frac{p}{2}$. As such, a cardinal property of the isotropic RW is that the next position solely depends on the current. This is the ever-common Markov property – that is to say, random walks are memoryless and stochastic – and it is what allows us to formulate RW dynamics as a transition probability matrix, or a *Markov chain*. This useful Markovian formulation is at the core of nearly all questions posed in the literature thus far, and in this and subsequent chapters we too will use this formulation to derive many features of RWs.
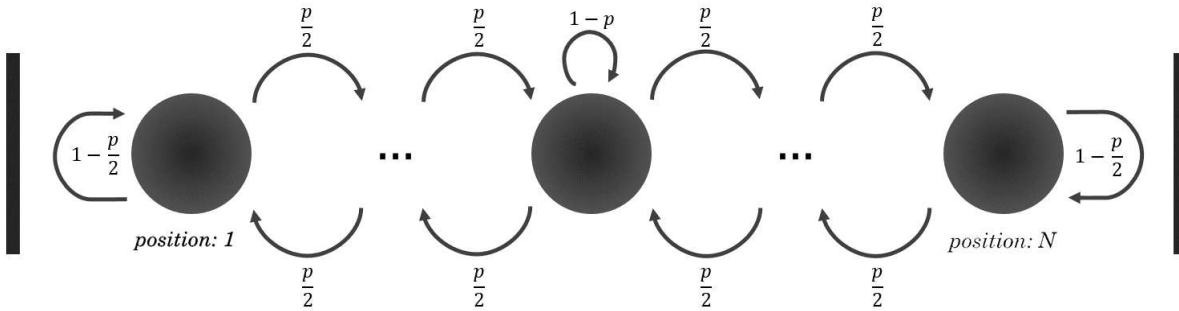

Figure 2.1: Rules for the reflective 1D symmetric walk. A D-dimensional walk aggregates D perpendicular instances of this. This is a recreation of a graphic by Franklin [2018].

Extrapolating these dynamics to a higher dimension D reduces the movement probabilities to $\frac{p}{2D}$ while the probability of a standstill remains $1 - p$. Deliberately chosen for this research is the *reflective* boundary condition, where moving left off the left edge reverses motion perpendicular to the boundary; the boundary standstill probability therefore rises to $1 - \frac{p}{2D}$. Assuming independence between directional choice for all D dimensions these dynamics allow the walker to move diagonally for $D = 2$ (classifying the algorithm as a *next-nearest-neighbour* walker, explained graphically in Figure 2.2) and to step onto any of the 3^D adjacent positions for arbitrary dimensions.

A possible variable in this work is the neighbourliness of the algorithm. An equally valid walking con-

dition assumes mutual exclusivity for movement choices between dimensions such that diagonal moves are prohibited. Walkers that move like this are known as *nearest-neighbour* (NN) walkers and contrast the algorithm outlined previously, known as the *next-nearest-neighbour* (NNN) algorithm, although of course there is no difference for $D = 1$. An exemplar 2D depiction of this, valid for the bulk of the lattice, is displayed in Figure 2.2. This research will only investigate the next-nearest case although references to the NN case will be mentioned where relevant.
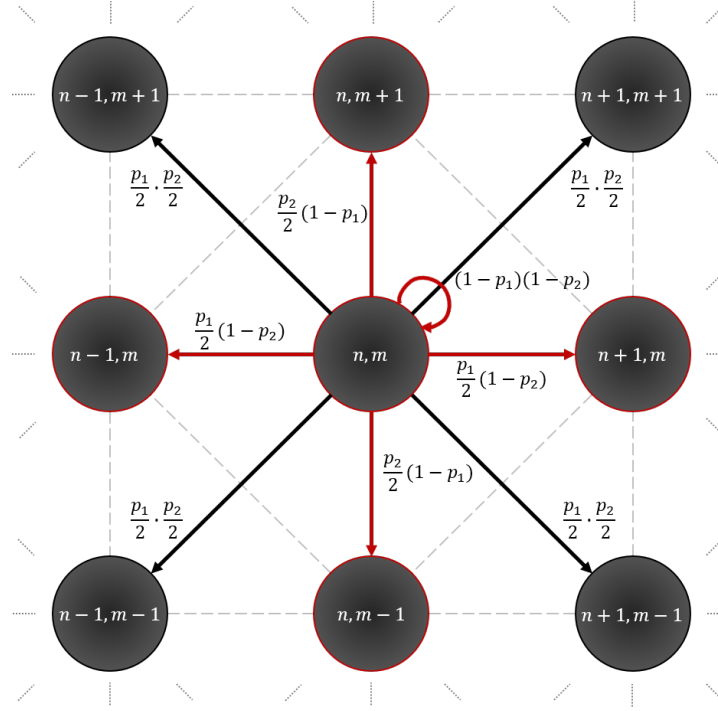

Figure 2.2: The set of movement choices for the 2D, isotropic, **(red)** nearest-neighbour walk and **(red & black)** next-nearest-neighbour walk in the bulk of the lattice. This is a recreation of a graphic by Franklin [2018].

Also considered in other papers is the lattice configuration; a lot of related scientific literature, especially older papers, carried out their analysis on different types of integer lattices. For example Vineyard [1963] looks at an asymptotic form of the number of new site visitations for three different lattice arrangements. The three main variations are the body-centred cubic, the face-centred cubic, and the primitive cubic – their defining unit cells are shown in Appendix Figure A.1. This dissertation will only focus on primitive cubic lattices, as does the large majority of modern research.

For the one-dimensional lattice – sometimes referred to as a *number line* – the Markov chain defining transition probabilities for the confined interval $[1, N]$ is the perturbed, tridiagonal $N \times N$ matrix

$$
\boldsymbol{P} = \begin{bmatrix}
1 - \frac{p}{2} & \frac{p}{2} & 0 & \dots & 0 \\
\frac{p}{2} & 1 - p & \frac{p}{2} & \dots & 0 \\
0 & \frac{p}{2} & 1 - p & \dots & 0 \\
\vdots & \vdots & \vdots & \ddots & \vdots \\
0 & 0 & 0 & \dots & 1 - \frac{p}{2}
\end{bmatrix}.
$$

This can now be used to find the *occupational probability function*, $P_{n_0} = P_{n_0}(N, n, p, t)$. This describes the analytic probability of a random walker, originating at n_0, occupying node n at time t – other vari-

ables influencing this are the length N of the 1D lattice and the movement probability p, as the function incorporates both reflective boundaries and the possibility of a standstill. This is wholly a result of recent work on finding eigenvalues of tridiagonal matrices such as $\boldsymbol{P}$ [Yueh, 2005] and on discrete propagator functions [Giuggioli, pp]. Detailing these derivations in full is beyond the purview of this report – we only introduce this lightly, and instead primarily focus on the utility of their results.

The *eigendecomposition* (or *diagonalisation*) of $\boldsymbol{P}$ is the first important step in the derivation of P_{n_0}. We construct a square matrix $\boldsymbol{V}$ whose columns are the eigenvectors of $\boldsymbol{P}$:

$$\boldsymbol{V} = \begin{bmatrix} \boldsymbol{v}_1 & \cdots & \boldsymbol{v}_N \end{bmatrix},$$

$$= \begin{bmatrix} v_{1,1} & v_{2,1} & \cdots & v_{N,1} \\ v_{1,2} & v_{2,2} & \cdots & v_{N,2} \\ \vdots & \vdots & \ddots & \vdots \\ v_{1,N} & v_{2,N} & \cdots & v_{N,N} \end{bmatrix}.$$

We next assemble the eigenvalues of $\boldsymbol{P}$ in a diagonal matrix $\boldsymbol{J}$ such that the kth diagonal λ_k is the eigenvalue associated with the kth eigenvector of $\boldsymbol{V}$:

$$\boldsymbol{J} = diag\{\lambda_1, \lambda_2, \ldots, \lambda_N\},$$

$$= \begin{bmatrix} \lambda_1 & \cdots & 0 \\ \vdots & \ddots & \vdots \\ 0 & \cdots & \lambda_N \end{bmatrix}.$$

Finally we combine $\boldsymbol{V}$ and $\boldsymbol{J}$ in the following manner:

$$\boldsymbol{P} = \boldsymbol{V}\boldsymbol{J}\boldsymbol{V}^{-1},$$

$$= \begin{bmatrix} v_{1,1} & v_{2,1} & \cdots & v_{N,1} \\ v_{1,2} & v_{2,2} & \cdots & v_{N,2} \\ \vdots & \vdots & \ddots & \vdots \\ v_{1,N} & v_{2,N} & \cdots & v_{N,N} \end{bmatrix} \begin{bmatrix} \lambda_1 & \cdots & 0 \\ \vdots & \ddots & \vdots \\ 0 & \cdots & \lambda_N \end{bmatrix} \begin{bmatrix} v_{1,1} & v_{2,1} & \cdots & v_{N,1} \\ v_{1,2} & v_{2,2} & \cdots & v_{N,2} \\ \vdots & \vdots & \ddots & \vdots \\ v_{1,N} & v_{2,N} & \cdots & v_{N,N} \end{bmatrix}^{-1}.$$

This diagonalised form has the valuable property that enables

$$\boldsymbol{P}^t = \boldsymbol{V}\boldsymbol{J}^t\boldsymbol{V}^{-1},$$

$$= \boldsymbol{V} \begin{bmatrix} \lambda_1^t & \cdots & 0 \\ \vdots & \ddots & \vdots \\ 0 & \cdots & \lambda_N^t \end{bmatrix} \boldsymbol{V}^{-1},$$

which we use to propagate the initial condition $P_{n_0}(N, n, p, t = 0)$ forward in time and across the entire lattice. Mathematically, this is done by raising $\boldsymbol{P}$ to the power t and then multiplying by the initial condition $P_{n_0}(N, n, p, 0)$. Using index notation this is

$$P_{n_0}(N, n, p, t) = \sum_{i=1}^{N} \sum_{j=1}^{N} \boldsymbol{V}_{ij} \boldsymbol{J}_{jj}^t \boldsymbol{V}_{ji}^{-1} P_{n_0}(N, n, p, 0).$$

In accordance with Giuggioli [pp], this can be expressed as the following function in which each summand corresponds to an eigenvalue of the system:

$$P_{n_0}(N, n, p, t) = \frac{1}{N} \sum_{k=1}^{N} \alpha_k \cos\left[(2n - 1)\frac{\pi(k - 1)}{2N}\right] \cos\left[(2n_0 - 1)\frac{\pi(k - 1)}{2N}\right] \lambda_k^t, \tag{2.1}$$

where the conditional variable

$$\alpha_k = \begin{cases} 1 & \text{if } k = 1, \\ 2 & \text{otherwise,} \end{cases} \tag{2.2}$$

and the N eigenvalues of $\boldsymbol{P}$ are denoted λ_k, $k = 1, 2, ..., N$ as before and are given by [Yueh, 2005] as

$$\lambda_k = 1 - p \left[1 - \cos \left(\frac{[k-1]\pi}{N} \right) \right]. \tag{2.3}$$

We note these equations require the lattice to be defined on the interval $[1, N]$. This is in opposition to the definition $[-N, N]$, which many simulations use in this paper for simplicity in programming. Whenever such results are consolidated with P_{n_0} we are careful to translate our coordinates accordingly.

Similarly, the transition probabilities for a 2D $M \times N$ lattice are represented by a 4D $M^2 \times N^2$ tensor – this is simply an $M \times N$ matrix where each element is an $M \times N$ daughter matrix.
The $(i, j)^{\text{th}}$ element in $\boldsymbol{P}^t$ represents the probability of walking from the ith to the jth node in t timesteps – likewise, the $(i, j, k, l)^{\text{th}}$ element of this 4D tensor raised to the power t (i.e. the $(k, l)^{\text{th}}$ element of the $(i, j)^{\text{th}}$ daughter matrix) holds the probability of walking from the $(i, j)^{\text{th}}$ to the $(k, l)^{\text{th}}$ lattice point in t timesteps. The corresponding propagator function for $D = 2$ is obtained analogously to the $D = 1$ case, with the added necessary assumption that movement in either dimension is independent. This yields:

$$P_{n_0, m_0}(N, M, n, m, p, t) = \frac{1}{NM} \sum_{k=1}^{N} \sum_{k'=1}^{M} \alpha_k \alpha_{k'} \cos \left[(2n-1) \frac{\pi(k-1)}{2N} \right] \cos \left[(2n_0 - 1) \frac{\pi(k-1)}{2N} \right]$$
$$\cos \left[(2m-1) \frac{\pi(k'-1)}{2M} \right] \cos \left[(2m_0 - 1) \frac{\pi(k'-1)}{2M} \right] (\lambda_k \lambda_{k'}')^t. \tag{2.4}$$

As we treat the new dimension as independent, we also define its own eigenvalues. As before, these are

$$\lambda_{k'}' = 1 - p_2 \left[1 - \cos \left(\frac{[k'-1]\pi}{M} \right) \right], \tag{2.5}$$

where p_2 and M are the equivalent of p and N through the second dimension. We give the generalised D-dimensional form in Appendix Equation (A.1).

How do these dynamics manifest in a D-dimension lattice? To answer this a Monte Carlo `MATLAB` program was written to generate $I = 10^3$ instances of random walks on a D-dimensional lattice for $D = 1, 2, 3$. The occupational probability was then calculated by normalising the resultant distribution of walkers. Figure 2.3 shows the evolution of occupational probabilities for $D = 2$ along with a comparison to the analytic results obtained by evaluating (2.4) at different coordinates. In all proceeding simulations, unless stated otherwise, all D movement probability parameters $p_1, ..., p_D$ are set to a single value p; this condition will be referred to as the *unanimous probability condition*.

One of the simplicities of 1D RWs is the lack of *parity issues*; these are what we encounter when walkers *must* move through all dimensions every timestep. Previous simulations used values of p sufficiently less than unity, however when $p_1, ..., p_D \to 1$ to within a tolerance of roughly 0.1 we force this phenomenon and thus increasingly observe these parity issues. They play a small role in coverage tasks – and more so in those with a directional correlation – due to the restriction they set on a walker's path. Such a walker is almost certainly constrained to a specific diagonal for $D > 1$ and will therefore struggle to visit nodes in other diagonals until it reaches the reflective boundary and attempts to move through it, but instead
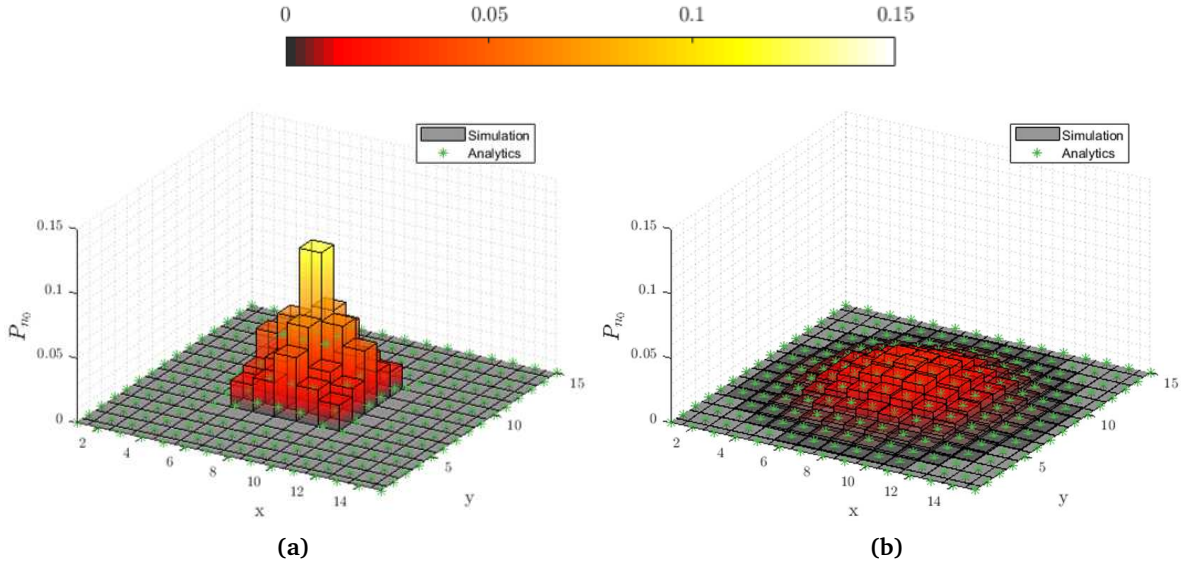
Figure 2.3: Occupational probabilities for a 15×15 lattice at timesteps **(a)** $t = 3$ and **(b)** $t = 8$, represented by both the height and colour of the histogram (the colourbar applies to both). Here $p_1 = p_2 = \frac{3}{4}$, walkers all start at the centre node $(8, 8)$, and the bars' face transparency was set to 60% so that analytic solutions are visible. Similar plots for the $D = 1, 3$ cases can be found in Appendix Figures A.2 and A.3 respectively.

shifts onto another diagonal. Consequently setting $p_1, p_2, \ldots, p_D \to 1$ for a $D > 1$ reduces coverage performance.

Some benign effects of parity become apparent before the negative issues manifest. When $p_1, p_2, \ldots, p_D \lesssim 0.99$, walkers are forced to exclusively occupy even-only lattice co-ordinates at odd timesteps (or even timesteps, of course depending on initial conditions) and vice versa for odd-only co-ordinates. These are just the nodes a next-nearest-neighbour walk can reach that a nearest-neighbour walk cannot – i.e. only the black nodes in Figure 2.2. We provide a visualisation of three slices corresponding to each of the planes through a 3D cubic lattice of length 25, showcasing the resultant grid-like distribution.
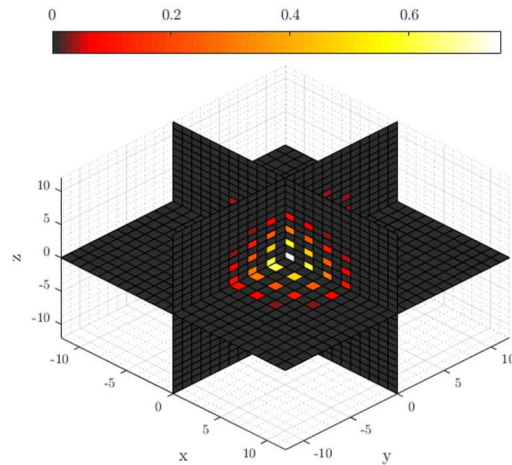

Figure 2.4: Parity effects for a $25 \times 25 \times 25$ lattice at $t = 10$ where $p = 1$ unanimously, averaged over $I = 10^5$ walks.

PATH ANALYSIS

In this chapter, we dedicate the first section to the challenge of separating a walk's occupational probability and its *first-passage probability* (FPP), which is the likelihood of a walk visiting a node at a given time for the first time. Historically, the FPP distribution of a walk has been notorious in its elusivity, though many closely-affiliated statistics and niche special cases have been solved for. Although now solved, for a long while the field of applied RWs has been aware of the difficulty of this calculation, and papers that attempt its obtention usually reflect on this. Works by Holcman et al. [2018] and Nagar and Pradhan [2003], for example, admit both the difficulty of the problem as well as the lack of generality in their solutions. The first of these examples looks at the first (and second) escape times for specific cellular geometries; this problem involves all the RW dynamics discussed already, with the added caveat that some portion of the boundary is absorptive, i.e. serves as an escape from the domain. This is a continuous-time application in which neurobiologists are particularly interested. Nagar and Pradhan's paper is on the scaling functions of FPP distributions in various discrete geometries [Nagar and Pradhan, 2003], and is unique in that its purpose seems to be recreational, though its results are tenable still.

The leading motives for first-passage time (FPT) research include calculating geometry- and solute-specific reaction constants for condensed matter systems [Grebenkov et al., 2018]. Indeed, the FPT distribution is a staple in statistical mechanics and computational chemistry papers – the same can also be said for its mean quantity, the *mean first-passage time* (MFPT), which has its own history and abundance of literature. The aforementioned research by Holcman et al. is an example of work inspired by condensed matter biochemistry. Other prevalent motives include the analysis of stochastic models where the FPT can be interpreted as a *survival time*; a historical example would be the famous gambler's ruin scenario (briefly mentioned in Chapter 1), but much more commonly these are found in biology where researchers are interested in processes such as the spreading of disease in a network or cell motility [Krummel et al., 2016]. Researchers in applications like these are primarily interested in minimising the FPT, as in the case of immune cell propagation, or maximising it, as with disease spreading.

Our contribution to the literature is in our theoretical analysis on RW propagation using the Z-transform, often introduced alongside the Laplace transform for their common uses, integrated with a lesser-known algorithm for its inversion back onto the time domain. We adapt the algorithm with specificity to our work, taking special care for parameters to fall only within valid ranges. More specifically, we compute

a near approximation to the FPP distribution of a symmetric walker with a standstill probability in the reflective, primitive, cubic-bound, $\mathbb{Z}^D$ lattice for $D = 1,2,3$ through numerical quadrature. Additionally, we verify the accuracy of our results with methods appropriate for each dimension $D \leqslant 3$.

In the second section we shift our focus to the enumeration of RW paths and the patterns therein, especially looking at the effects of varying dimensionality and boundary conditions. We also study the relation our results have to other well-known constructions, such as Pascal's triangle, and other well-studied phenomena, such as ballistic trajectories. Literature for this is sparse, and where it exists it is usually deeply technical and abstract [Andrews, 1990; Cicuta et al., 2002].

3.1 First passage

A useful mathematical object used ubiquitously in the advanced study of probability theory and signal processing is the Z-transform, sometimes called the generating function, of a distribution or signal. It can be likened to the Laplace transform as it too converts a time-series input $f(t)$ into a frequency-domain, complex representation $\hat{f}(z)$, the only difference being that Z-transforms are defined for discrete-time inputs. Insofar as obtaining a computable expression for the FPP distribution, precedent research has proved it useful to think of the occupational probability P_{n_0} in (2.1) as an input signal and the FPP distribution as our desired output [Zumofen and Blumen, 1982; Cicuta et al., 2002; Chupeau et al., 2015; Holcman et al., 2018; Yokoi et al., 1990].

The Z-transform itself, in the context of probability theory, is defined as

$$\hat{f}(z) = \sum_{t=-\infty}^{\infty} f(t)z^t, \quad z \in \mathbb{C}. \tag{3.1}$$

We now apply this to (2.1) to obtain the Z-domain occupational probability signal, finding it to be unilateral since $P_{n_0}(N,n,p,t) = 0$ for $t < 0$:

$$\mathscr{P}_{n_0}(N,n,p,z) = \sum_{t=0}^{\infty} P_{n_0}(N,n,p,t)z^t. \tag{3.2}$$

We simplify this using the identity for a geometric series in $z\lambda_k$ as

$$\sum_{t=0}^{\infty} (z\lambda_k)^t = \frac{1}{1-z\lambda_k}$$

to obtain

$$
\begin{aligned}
\mathscr{P}_{n_0}(N,n,p,z) &= \sum_{t=0}^{\infty} \frac{z^t}{N} \sum_{k=1}^{N} \alpha_k \cos\left[(2n-1)\frac{\pi(k-1)}{2N}\right] \cos\left[(2n_0-1)\frac{\pi(k-1)}{2N}\right] \lambda_k^t, \\
&= \frac{1}{N} \sum_{k=1}^{N} \alpha_k \cos\left[(2n-1)\frac{\pi(k-1)}{2N}\right] \cos\left[(2n_0-1)\frac{\pi(k-1)}{2N}\right] \sum_{t=0}^{\infty} z^t \lambda_k^t, \\
&= \frac{1}{N} \sum_{k=1}^{N} \frac{\alpha_k \cos\left[(2n-1)\frac{\pi(k-1)}{2N}\right] \cos\left[(2n_0-1)\frac{\pi(k-1)}{2N}\right]}{1-z\lambda_k}.
\end{aligned}
\tag{3.3}
$$

Extrapolation to a higher dimension D is straightforward and exemplified in Chapter 2, although we provide the generalised formula in Appendix Equation A.3. For the sake of concision we will now omit parameters implied by the lattice and introduce a small change in notation, vectorising n_0, n to $\boldsymbol{n}_0, \boldsymbol{n} \in \mathbb{R}^D$.

Now note that the t-domain propagator accounts for *all* walks starting at $\boldsymbol{n}_0$ and ending at $\boldsymbol{n}$; this allows us to split it into two parts. The first accounts for walkers' first passage to $\boldsymbol{n}$ and the second accounts for the remainder, i.e. all walks starting at $\boldsymbol{n}$ after the first-passage time t' and ending at $\boldsymbol{n}$ again at the original inquested time t, where $t > t'$. Assuming $\boldsymbol{n}_0 \neq \boldsymbol{n}$ we now have

$$P_{\boldsymbol{n}_0}(\boldsymbol{n}, t) = \sum_{\forall t' < t} F_{\boldsymbol{n}_0}(\boldsymbol{n}, t') P_{\boldsymbol{n}}(\boldsymbol{n}, t - t'),$$

where $F_{\boldsymbol{n}_0}(\boldsymbol{n}, t')$ is the first-passage probability function, whose output is the probability that a walk originating at $\boldsymbol{n}_0$ visits $\boldsymbol{n}$ at time t' for the first time. The constrained summation makes it difficult to extract $F_{\boldsymbol{n}_0}$ so we apply the Z-transform to all terms in the equation, as in (3.2), to give

$$\mathscr{P}_{\boldsymbol{n}_0}(\boldsymbol{n}, z) = \mathscr{F}_{\boldsymbol{n}_0}(\boldsymbol{n}, z) \mathscr{P}_{\boldsymbol{n}}(\boldsymbol{n}, z),$$

$$\mathscr{F}_{\boldsymbol{n}_0}(\boldsymbol{n}, z) = \frac{\mathscr{P}_{\boldsymbol{n}_0}(\boldsymbol{n}, z)}{\mathscr{P}_{\boldsymbol{n}}(\boldsymbol{n}, z)}. \tag{3.4}$$

Inverting this is possible through the complex Cauchy integral, which parallels the Bromwich integral used for Laplace inversions. This gives

$$F_{\boldsymbol{n}_0}(\boldsymbol{n}, t) = \frac{1}{2\pi j} \oint_{\Phi} \mathrm{d}z \; z^{-(t+1)} \mathscr{F}_{\boldsymbol{n}_0}(\boldsymbol{n}, z), \tag{3.5}$$

where Φ is a counterclockwise circular contour centred at the origin whose radius is within the region of convergence (ROC) of the signal F. Φ here is not necessarily a circle but by Cauchy's residue theorem using this contour simplifies our integral without loss of generality.

Following standard protocol for solving Cauchy integrals, knowledge of the ROC is required to proceed. The ROC is defined as the set of z values for which the Z-transform exists, i.e. doesn't blow up. Formally we write

$$\text{ROC} = \left\{ z : \left| \sum_{t=0}^{\infty} F_{\boldsymbol{n}_0}(\boldsymbol{n}, t) z^t \right| < \infty \right\},$$

$$= \left\{ z : \sum_{t=0}^{\infty} \left| F_{\boldsymbol{n}_0}(\boldsymbol{n}, t) \right| \left| z^t \right| < \infty \right\}.$$

Next we realise that while F is not precisely a normalised probability distribution as its probabilities need not have a unit sum, it is *bound* by a normalised probability distribution and so we are assured of its absolute summability;

$$\sum_{t=0}^{\infty} \left| F_{\boldsymbol{n}_0}(\boldsymbol{n}, t) \right| < \infty. \tag{3.6}$$

Also of use is the knowledge that the termwise product of two convergent series is also convergent. This can be proven by taking the infinite limit of their Cauchy product [Flygare, 2012]. With this and (3.6) we can proceed as follows:

$$\text{ROC} = \left\{ z : \sum_{t=0}^{\infty} \left| z^t \right| < \infty \right\},$$

$$= \left\{ z : \sum_{t=0}^{\infty} \left| \left(r e^{j\theta} \right)^t \right| < \infty \right\},$$

$$= \left\{ z : \sum_{t=0}^{\infty} \left| r^t \right| \left| e^{jt\theta} \right| < \infty \right\},$$

where we parametrised z using the polar co-ordinates r, θ as is standard for complex circulation integrals. Two elementary properties of polar co-ordinates then help us simplify this further; the first allows us to say that $\left| e^{jt\theta} \right| = 1$ always and the second states $r \geqslant 0$. We therefore know that

$$\text{ROC} = \left\{ z : \sum_{t=0}^{\infty} r^t < \infty \right\}.$$

Thus we conclude that the ROC is the complex unit disc about the origin, excluding its boundary $|z| = 1$. Finally, we can define simply

$$\text{ROC} = \{z : |z| < 1\}, \tag{3.7}$$

which agrees with a well-established result in signal processing. If we account for the opposing convention used by control engineers – who use $-t$ as their z exponent – then this result is consistent with the fact that the ROC of causal signals is known to be the exterior of some complex circle $|z| = R$. Causal signals are those whose value is null for negative t; most real-time sound filters are causal for example, whereas image processing filters are acausal generally. To parallel the Laplace transform too, this can be equated to a pole's positioning on the left half-plane of a pole-zero plot.

Continuing with the computation of (3.5) we must now incorporate (3.7) into any of the plethora of integral inversion procedures readily available online. The one likely best-suited for us comes from the all-encompassing work of Whitt et al. [2000] on the applications of numerical inversions.

Z-transforms are chiefly used by control engineers, who typically work with rational functions. These are generally readily invertible symbolically and so most sources recommend using computer algebra software (CAS). CAS works best with polynomials and differential equations – often encountered when working with transfer functions – but for our purposes and for many statisticians most CAS is unsuitable as generating functions are seldom neat and in a form that's easy to parse. Nevertheless, some CAS (including that of `MATLAB`) are robust enough to manipulate (3.5). We discard these regardless; not only are they a black-box approach – universally frowned upon in mathematics – but their output is, more often than not, ill-suited for further analysis [Fateman and Kahan, 2000]. Many sources provide alternatives to CAS, some recommending that we tackle Equation (3.5) using Cauchy's residue theorem. This is possible only for the 1D RW and only two known methods exist; the first coincides with the classic solution to the 1D coverage problem by Nemirovsky et al. (see Section 1.1) and the second, much more recent method involves reducing our F_{n_0} to a Chebyshev polynomial and manipulating its roots [Giuggioli, pp]. We use the latter to validate our results, though its underlying mathematics is omitted as it forms an integral part of a paper currently under review.

Other candidate methods for higher-dimension inversions involve generic Fourier inverse transforms, largely due to their similarities to the Z-transform. General solutions like this are inattentive though and allow much room for error. Whitt et al. remedy this by collating a lot of prior papers (largely their own) to build a robust inversion algorithm, delineated in their Section 1.2.4. Their algorithm is especially suited for us as it can be easily adapted to the ROC we calculated earlier. The FPP distributions for $D = 1, 2, 3$ are visualised appropriately using `MATLAB` in Figure 3.1.
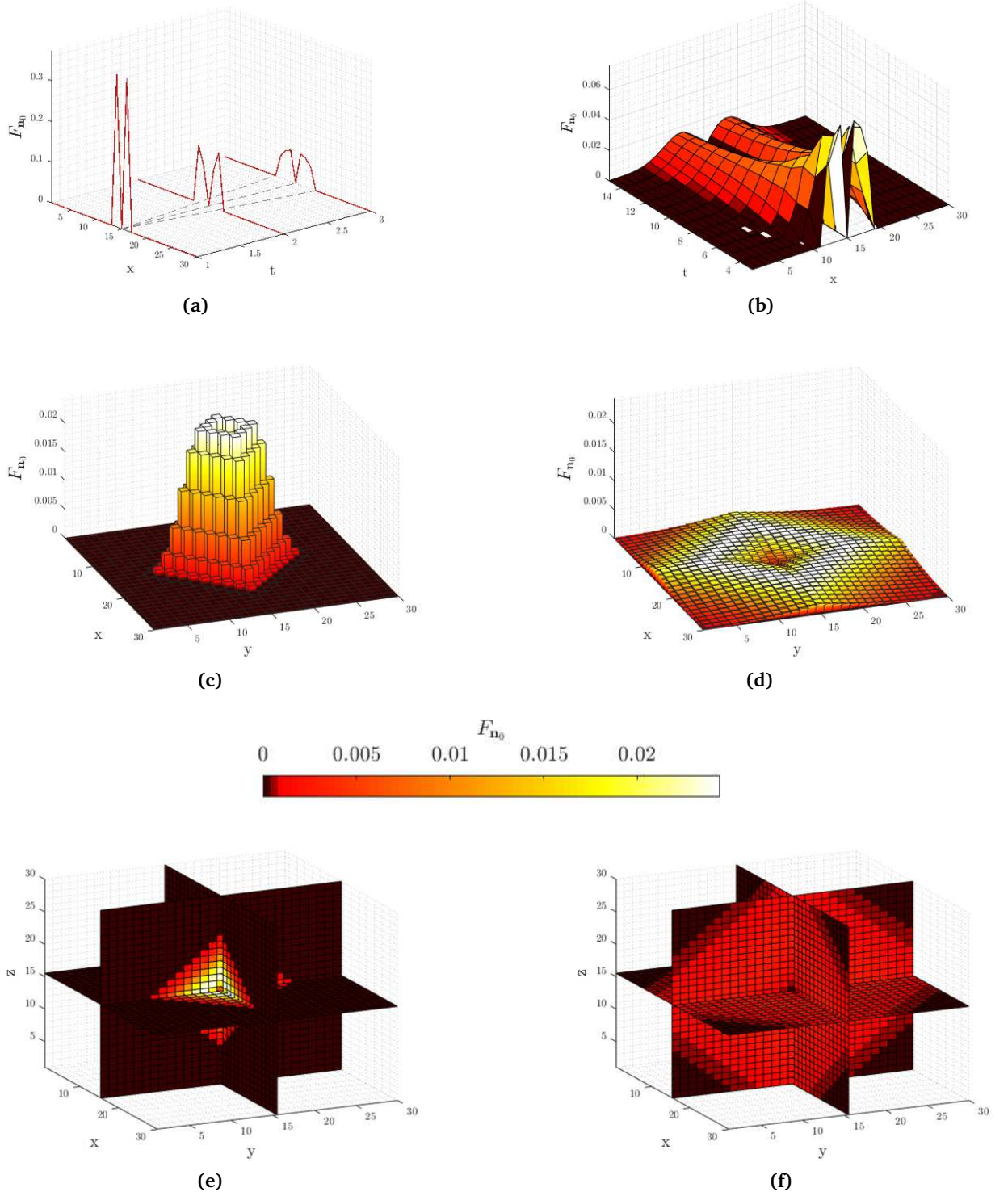
Figure 3.1: The FPP distribution, where $p = \frac{3}{4}$ and the walk starts at the centre of the lattice, for **(a,b)** the 1D lattice [1,30], **(c,d)** the 30×30 lattice, and **(e,f)** the $30 \times 30 \times 30$ lattice. **(a)** We draw three semi-transparent grey lines for reference; one marks the starting node n_0 to show all FPPs are null there and the other two show the diagonal lines that mark the one-step-per-timestep limit. **(b)** We show separately the next 12 timesteps (i.e. $3 \leqslant t \leqslant 15$) as a colour-valued surface for clarity. The small white regions are sub-zero probabilities; these are aliasing errors that occur near areas of steepness as a consequence of discretisation. The 2D distribution is shown at **(c)** $t = 10$ and **(d)** $t = 100$. The 3D case is shown for **(e)** $t = 10$ and **(f)** $t = 100$ too, with slices taken through the centre. Algorithm parameters are $l = 1, r = 10^{-4/t}$ to agree with the ROC $|z| < 1$ when $t > 0$.

Figure 3.1a shows only the first 3 timesteps for clarity. These reveal two prominent peaks whose height is found to be dependent on p; during the first timestep, with n_0 occupied, only $n_0 - 1$ or $n_0 + 1$ can be visited for the first time, each with probability $\frac{p}{2}$. This agrees with the observed peaks at $t = 1$, whose heights are indeed $\frac{p}{2} = 0.375$. In subsequent timesteps these peaks see a gradual height decay which we might expect to observe everywhere. In fact, we can show this height decay is not only present everywhere, but its rate is both inversely proportional to $|\boldsymbol{n} - \boldsymbol{n}_0|$ and directly proportional to p. To thoroughly study this, we look at the FPP between two fixed endpoints, letting t be our independent variable rather than the target node $\boldsymbol{n}$. Given the difficulty of clearly illustrating temporal FPP trends for $D > 1$, this method is found to be especially advantageous when looking at trends varying with the endpoints' positions, when looking at these positions qualitatively.

In Figure 3.2 we compare $F_{\boldsymbol{n}_0}$ in a cubic lattice to substantiate our prior claim about FPP decay. Our starting position $\boldsymbol{n}_0 = (n_0, m_0, s_0)$ is the centre of an $N \times M \times S$ cube, and we compare targets at the centre of a face $\boldsymbol{n} = (N, m_0, s_0)$, at the centre of an edge $\boldsymbol{n} = (N, M, s_0)$, and at a corner $\boldsymbol{n} = (N, M, S)$. Therein, we show the distribution has two timescales.

The first timescale corresponds to a freely-propagating walk. It begins (that is, the curve separates from $F_{\boldsymbol{n}_0} = 0$) at approximately $\frac{2|\boldsymbol{n} - \boldsymbol{n}_0|}{p}$. This is because every timestep has probability $\frac{p}{2}$ of incurring a move in the direction of the target $\boldsymbol{n}$, regardless of dimensionality and direction due to symmetry. These dynamics start to weaken while the second timescale takes over. The second timescale is enacted around the time first contact with the boundary is made – again, this time is inversely proportional to p for the same reasons. This later timescale is what pulls the FPP down to its asymptotic value as it represents the ensemble of possible walks spreading evenly across the domain. Due to symmetry, it follows that this asymptotic value is $\frac{1}{V}$ where V is the volume of the lattice; we affirm this mathematically in Section 3.2. We also affirm p behaves only as a scaling parameter in both timescales in Appendix Figure A.12.

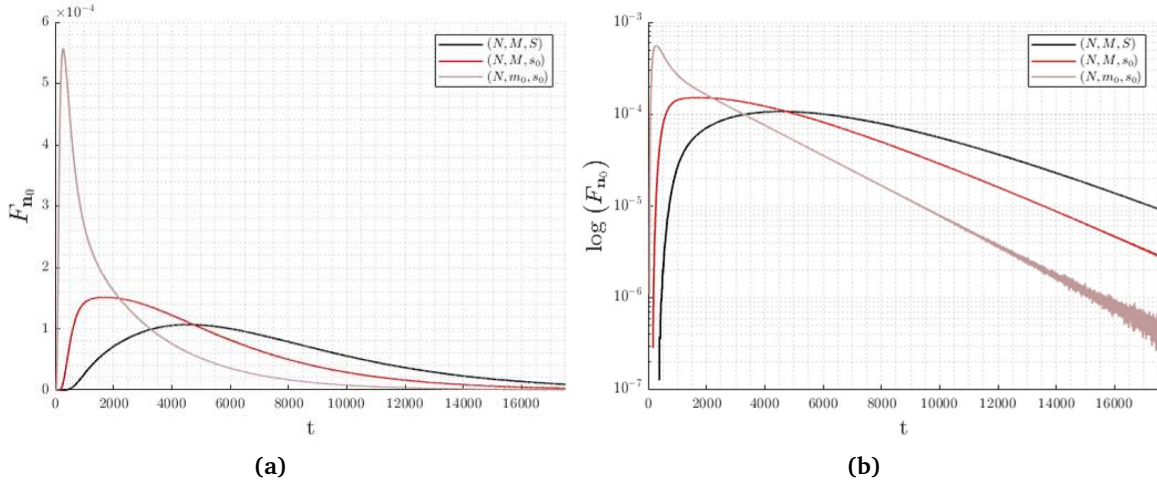**(a)**   **(b)**

Figure 3.2: FPP distribution of a $50 \times 50 \times 50$ cubic lattice, where $p = \frac{3}{4}$ unanimously, between the centre and three distinct targets. Numeric gradient values are stored in Appendix Table A.1, though the inverse relationship between the decay rate and $|\boldsymbol{n} - \boldsymbol{n}_0|$ can be seen here directly. Large-t fluctuations are actually smaller than earlier ones, but they are a larger proportion of the function's magnitude – this becomes apparent when the vertical axis is log-scaled. This is amplified as the values approach MATLAB's double-precision limit.

3.1.1 Validity of results

While Whitt et al. provide an error bound and an error approximation, these only consider aliasing errors as a result of discretising the z-domain. They predict a bound of $5p \times 10^{-9}$ for any inversion; we show in this subsection this is not the complete picture and other errors are present.

We gauge the accuracy of our inversion in 1D by comparing the time series output to the time series output from the analytic FPP distribution. This is from a paper soon to be published [Giuggioli, pp]. For higher dimensions this is not available, hence we choose to compare moments of the distribution. For 2D we obtain the factorial moments of the distribution and convert them to a scale-invariant form for easier comparability and reproducibility. This is done by differentiation which, normally, would utilise a numeric differentiator resulting in some non-negligent error. Of course, this renders error analysis ineffective; to mitigate this we use CAS differentiation and substitution – notwithstanding round-off errors, there are no inaccuracies associated with this. For 3D we must accept some inexactitude; the formula we employ is derived from an infinite sum, so naturally its computable form is accompanied by a truncation error. Conveniently, this also means we know the error's order of magnitude. This method is not available for 2D space for reasons related to 3D transience.

3.1.1.1 For one dimension

As mentioned already, the 1D FPT distribution is attainable analytically [Giuggioli, pp]. Fully expanded, the Cauchy inversion integral is

$$F_{n_0}(n,z) = \frac{1}{2\pi j} \oint_\Phi \mathrm{d}z\, z^{-(t+1)} \frac{\displaystyle\sum_{k=1}^{N} \frac{\alpha_k \cos\left[(2n-1)\frac{\pi(k-1)}{2N}\right] \cos\left[(2n_0-1)\frac{\pi(k-1)}{2N}\right]}{1-z\lambda_k}}{\displaystyle\sum_{k=1}^{N} \frac{\alpha_k \cos^2\left[(2n-1)\frac{\pi(k-1)}{2N}\right]}{1-z\lambda_k}} \tag{3.8}$$

Giuggioli was able to manipulate this into a ratio of Chebyshev polynomials. The roots of the denominator polynomial then give the poles of (3.8), from which the residues can be calculated easily. Then, in conjunction with Cauchy's residue theorem, (3.8) is factorised and transformed back into the time domain. The end result is conditional on the relative positioning of n and n_0:

$$F_{n_0}(n,t) = \begin{cases} \displaystyle\sum_{m=1}^{n-1} \frac{2(-1)^{m+1}p}{2n-1} \left|\sin\left[\Psi^+\right]\right| \cos\left[\frac{2n_0-1}{2}\Psi^+\right] \left(1-p+p\cos\left[\Psi^+\right]\right)^{t-1} & \text{if } n > n_0, \\[4ex] \displaystyle\sum_{m=1}^{N-n} \frac{2(-1)^{m+1}p}{2(N-n)+1} \left|\sin\left[\Psi^-\right]\right| \cos\left[\frac{2(N-n_0)+1}{2}\Psi^-\right] \left(1-p+p\cos\left[\Psi^-\right]\right)^{t-1} & \text{if } n < n_0, \end{cases} \tag{3.9}$$

where $\Psi^+ = \frac{2m-1}{2n-1}\pi$ and $\Psi^- = \frac{2m-1}{2(N-n)+1}\pi$.

This can be implemented directly onto `MATLAB`. Figure 3.3 compares this implementation with our numerical results. We see a good agreement between the two overall; our implementation is correct to a minimum of 5 decimal places initially, and to at least 7 for $t \gg 1$.

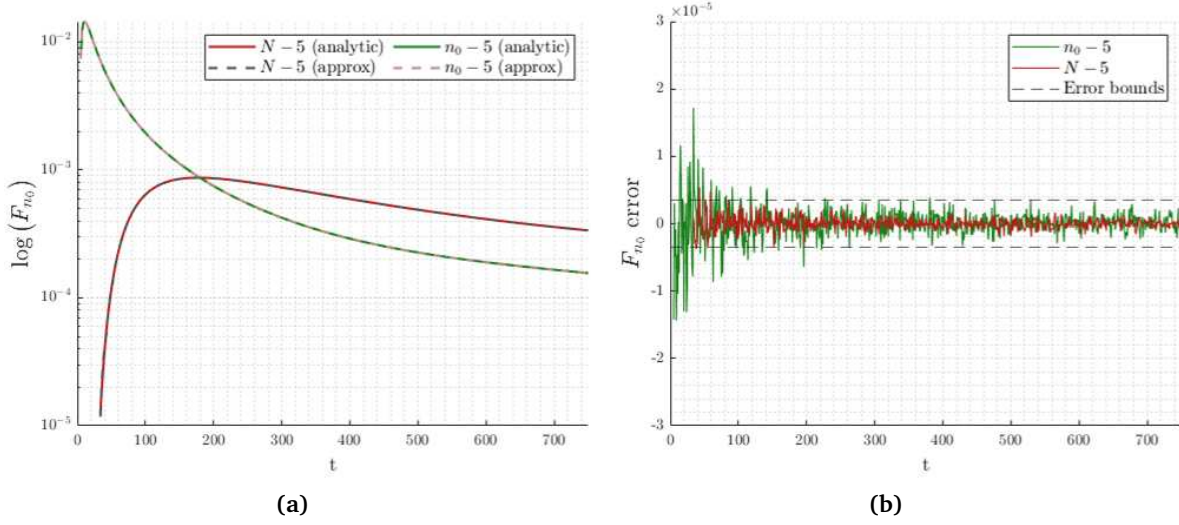**(a)**   **(b)**

Figure 3.3: Error analysis for our 1D numeric inversion, on a number line of length $N = 50$ where $n_0 = 25$ and $p = \frac{3}{4}$. The absolute errors are well-behaved and, while they do not converge to 0, their fluctuations are bound by approximately 3.5042×10^{-6} for $t > 300$.

3.1.1.2 For two dimensions

One of the Z-transform's main utilities is the ease with which we can calculate fundamental properties of the transformed signal. Evaluating, for example, the first derivative at $z = 1$ gives us the first moment, i.e. the expectation, of $f(t)$:

$$\left. \frac{\partial \hat{f}(z)}{\partial z} \right|_{z=1} = \sum_{t=-\infty}^{\infty} t f(t) = \mathrm{E}(t). \tag{3.10}$$

Generalising the above, we see the kth derivative at $z = 1$ gives the kth *rising factorial* moment (the first rising factorial moment is interchangeable with the first raw moment):

$$
\begin{aligned}
\left. \frac{\partial^k \hat{f}(z)}{\partial z^k} \right|_{z=1} &= \sum_{t=-\infty}^{\infty} t(t+1)\cdots(t+k-1) f(t), \\
&= \mathrm{E}\left[t(t+1)(t+2)\cdots(t+k-1) \right], \\
&= \mathrm{E}\left[\frac{(t+k-1)!}{(t-1)!} \right],
\end{aligned}
\tag{3.11}
$$

where the rising factorial expression $\frac{(t+k-1)!}{(t-1)!} = t(t+1)\cdots(t+k-1)$ is conventionally expressed as $t^{(k)}$. From this we can extract the kth raw moment $\mathrm{E}[t^k]$ by utilising the (unsigned) *Stirling numbers of the first kind*. These are defined by 2 input integers – k, s in this paper – and are most often used in combinatorics where they show the number of permutations of k items with s disjoint cycles (a graphical interpretation of this is shown in Appendix Figure A.11). Their origin however is with the factorial function as we use them here; they are the coefficients of the rising factorial when expanded as

$$
\begin{aligned}
t^{(k)} &= t(t+1)(t+2)\cdots(t+k-1), \\
&= \sum_{s=0}^{k} \begin{bmatrix} k \\ s \end{bmatrix} t^s,
\end{aligned}
$$

17

where $\begin{bmatrix} k \\ s \end{bmatrix}$ is the notation we will use for the Stirling numbers of the first kind. Exploiting the linearity of the expectation function E, we can state $\mathrm{E}[t^{(k)}]$ as a sum of the expectations of the raw moments up to k:

$$\mathrm{E}[t^{(k)}] = \sum_{s=0}^{k} \begin{bmatrix} k \\ s \end{bmatrix} \mathrm{E}[t^s],$$

We however are interested in the *standardised* moments $\widetilde{\mu}_k$; these describe the shape of the distribution when considered from the mean rather than from the origin and as a proportion of σ^k, where σ is the standard deviation. We do this so that our results are invariant to any scaling, for reproducibility – as disucssed earlier our movement parameter p is an example of a scaling variable.

The kth standardised moment is defined as $\widetilde{\mu}_k = \frac{1}{\sigma^k} \int_{\mathbb{R}} \mathrm{d}t \; (t-\mu)^k f(t)$ where μ is the mean. The general conversion between raw and standardised moments is well-known, and if we denote the kth raw moment μ'_k then it is given by

$$\widetilde{\mu}_k = \frac{1}{\sigma^k} \sum_{r=0}^{k} \binom{k}{r} (-1)^{k-r} \mu'_r \mu^{k-r},$$

where $\binom{k}{r}$ is the *choose* function for binomial coefficients and $\mu \equiv \mu'_1$ is still the mean. Knowing this, we find the standardised moments for $k \leqslant 4$ in terms of the rising factorial moments only:

$$\widetilde{\mu}_1 = 0, \tag{3.12a}$$

$$\widetilde{\mu}_2 = 1, \tag{3.12b}$$

$$\sigma^3 \widetilde{\mu}_3 = \mathrm{E}[t^{(3)}] \; - \; 3\mathrm{E}[t^{(2)}](1+\mu) \; + \; \mu + 3\mu^2 + 2\mu^3, \tag{3.12c}$$

$$\sigma^4 \widetilde{\mu}_4 = \mathrm{E}[t^{(4)}] \; - \; 2\mathrm{E}[t^{(3)}](3+2\mu) \; + \; \mathrm{E}[t^{(2)}](7+12\mu+6\mu^2) \; - \; \mu - 4\mu^2 - 6\mu^3 - 3\mu^4. \tag{3.12d}$$

Here $\mu := \mathrm{E}[t^{(1)}]$ and $\sigma := \sqrt{\mathrm{E}[t^{(2)}]}$, and we know $\mathrm{E}[t^{(s)}]$ for $s = 1,2,3,4$ are calculable via differentiation of the generating function, as in Equation (3.11). This operation is perfectly suited for the in-built CAS in `MATLAB`; the outcome is tabulated in Table 3.1, showing a successful average relative error of 1.2%.

These results agree qualitatively with our findings too. The third standardised moment $\widetilde{\mu}_3$ is given the name *skewness* for its measure of skew/tailedness about the mean. As a rule of thumb a positive skew indicates a mean greater than the median; this is indeed the case for us, as demonstrated in Appendix Figure A.4. $\widetilde{\mu}_4$ is known as *kurtosis*, and distributions whose $\widetilde{\mu}_4$ is less than that of a Gaussian are called *platykurtic*; the Gaussian kurtosis is 3 exactly and so our distribution falls in this category. Platykurtic distributions exhibit tails thinner than Gaussian tails; this is indeed the case for us, evidenced in Appendix Figure A.4.

k	Numeric inversion	CAS differentiation
1	0	0
2	0.9993	1
3	0.6959	0.7164
4	2.1882	2.2011

Table 3.1: $\widetilde{\mu}_k$ values when calculated via the numeric Z-transform inversion and via CAS differentiation of (3.8) in `MATLAB`. Computations performed on a 30×30 lattice where $p = 1$ unanimously, between $\boldsymbol{n}_0 = [15\ 15]$ and $\boldsymbol{n} = [30\ 15]$.

3.1.1.3 For three dimensions

Bénichou et al. [2005] also attempt the analytic obtention of first-passage times. In doing so, they find the kth raw moment of the FPP distribution in 3D space to be

$$\left\langle \mathbf{T}^k \right\rangle = k! N^k \left[\left(H(\boldsymbol{r}_T | \boldsymbol{r}_T) - H(\boldsymbol{r}_T | \boldsymbol{r}_S) \right) \left(H(\boldsymbol{r}_T | \boldsymbol{r}_T) - \overline{H} \right)^{k-1} + \mathcal{O}(kN^{-\frac{2}{3}}) \right]. \tag{3.13}$$

Here N is the number of nodes in the lattice and $\boldsymbol{r}_T, \boldsymbol{r}_S$ represent the target and starting nodes respectively. Our analysis will ignore the higher-order terms. The key part of the equation however is H, a *discrete pseudo-Green's function*, and its affiliate $\overline{H}$. *Green's functions* are a class of functions that extend the superposition principle often applied to algebraic and first-order differential equations, and are commonly used in solving boundary value problems. $H, \overline{H}$ lack a clear physical meaning and the authors only published their exact forms in a correctional note a year later [Bénichou and Condamin, 2006], a testament to the difficulty of this problem. The explicit forms of $H, \overline{H}$ are also only derived for 2D walks and, while a 3D derivation is beyond this project's scope, highly accurate estimates are provided in the paper, with an error of order $\mathcal{O}(kN^{-\frac{2}{3}})$ only, under certain assumptions.

k	Numeric inversion	Green's function	$kN^{-\frac{2}{3}}$
1	1.4915	1.4909	4×10^{-4}
2	4.4282	4.4388	8×10^{-4}
3	19.0130	19.8240	1.2×10^{-3}
4	115.0446	118.0462	1.6×10^{-3}

Table 3.2: $\tilde{\mu}_k$ values when calculated via the numeric Z-transform inversion and via Bénichou's method, normalised by $(NMS)^k$ where N, M, S are the lengths of each side of the cube. Computations performed on a $50 \times 50 \times 50$ cube where $p = 1$ unanimously, between $\boldsymbol{n}_0 = [25 \ 25 \ 25]$ and $\boldsymbol{n} = [40 \ 35 \ 30]$.

We use the output of (3.13) the same as that of (3.12) in 2D. The values are given in Table 3.2, and again show good agreement with an average relative error of 1.8%.

3.2 Path enumeration

Starting with the $D = 1$ case, it is expedient to enumerate paths on the number line through a position-versus-timestep table, where the flow of time is represented by the upward direction. Starting from first principles, we assume nothing but the knowledge that in one timestep the only movement possibilities are *left*, *right*, or *standstill*. It then follows that to completely enumerate all paths we should continue by iteratively defining any element as the sum of only the three elements directly below it. This stems from both the RW's Markov property – discussed in Chapter 2 – and from the property of *time reversibility*.

While time reversibility may seem an obvious observation, it does not hold for all Markov processes and proof beyond a surface-level inspection is appropriate. Formally, we are testing for a property known as *detailed balance,* which in turn implies time reversibility. Generally a symmetric transition matrix is not enough to guarantee this, and we test for it using the process' *stationary* or *equilibrium* distribution. We denote this by the row vector $\boldsymbol{\pi} \in \mathbb{R}^N$ to match the lattice's length N. We judge our Markov process time-reversible if and only if $\boldsymbol{\pi}, \boldsymbol{P}$ satisfy

$$\boldsymbol{\pi}_i \boldsymbol{P}_{ij} = \boldsymbol{\pi}_j \boldsymbol{P}_{ji}, \tag{3.14}$$

where $\boldsymbol{\pi}_i$ is the equilibrium probability of occupying node i. Bearing in mind that $\boldsymbol{P}$ is symmetric, we reason that as $t \to \infty$ the reflectivity of our lattice determines the equilibrium distribution to be

$$\boldsymbol{\pi} = \begin{bmatrix} \frac{1}{N} & \frac{1}{N} & \cdots & \frac{1}{N} \end{bmatrix},$$

and so we see that (3.14) is satisfied. Two alternative proofs, one of which invokes the occupational probability function P_{n_0}, are in Appendix B. Now proven for the 1D case, we can generalise this to any dimensionality of the NNN walk by reasoning that it is just a composition of D perpendicular, non-interacting, independent instances of the 1D case.

Proceeding, if we index our spatial position with x (on the horizontal axis) and temporal position with t (on the vertical axis) our recursive equation is

$$\xi(x,t+1) = \xi(x-1,t) + \xi(x,t) + \xi(x+1,t), \tag{3.15}$$

with the following necessary conditions:

$$\xi(0,0) = 1, \tag{3.15a}$$

$$\xi(x,t) = 0 \quad \text{for} \quad \forall t < 0, \tag{3.15b}$$

which respectively correspond to the starting position of ξ and the non-negative time domain of ξ. For our bounded lattice defined as the closed interval $[-N, N]$ we include the additional boundary condition

$$\xi(x,t) = 0 \quad \text{for} \quad \forall |x| > N, \tag{3.15c}$$

which forces ξ to lose translational invariance.

Through its sum of preceding terms our construction can be thought of as analogous to Pascal's triangle – famed even outside of mathematic circles – in which Fibonacci numbers, triangular numbers, powers of 11, and many more sequences are ingrained. Our only assumption necessitates the construction be in the form of a triangular array too, and if displayed base-down we get:

We now notice our construction and Pascal's triangle have many intersecting properties. The first and most seminal of these is that the terms of each layer t are the coefficients of the trinomial expansion

$$(1 + x + x^2)^t = \sum_{k=-t}^{t} \xi(k,t) x^{t+k},$$

just as Pascal's triangle is determined by the coefficients of the binomial expansion $(1 + x)^t$. For this reason Table 3.3 is often called *trinomial triangle*.

-3	-2	-1	0	1	2	3
			1			
		1	1	1		
	1	2	3	2	1	
1	3	6	7	6	3	1

Table 3.3: Array enumerating the paths RWs can take to a position on the number line when $t \leqslant 3$. Shown upside down for its resemblance to Pascal's triangle, also commonly shown base-down.

Some more inexhaustive similarities follow. Each row, if its entries are taken as digits and entries over 9 are carried over accordingly, spells a power of 111 such that the tth row, digit-by-digit, spells 111^t – just as the tth row in Pascal's triangle spells 11^t. The tth row also sums to 3^t, similarly to how rows in Pascal's triangle sum to corresponding powers of 2. The squares of the tth row sums to the middle entry

in row $2t$ for both triangles. The leading diagonals of both triangles are always 1. The second diagonals list the natural numbers $\mathbb{N}$. The third diagonals list the triangular numbers T_t, the fourth diagonals the tetrahedral numbers, and so on for higher-dimensional simplices (generalisations of the triangle). Both approximate the normal distribution as their number of rows approach infinity. If left-justified, the subsequent diagonals in Pascal's triangle sum to Fibonacci numbers; likewise the diagonals of the left-justified trinomial triangle sum to terms in a similar sequence which sums the previous *three* terms (starting with $\{0,0,1\}$). Many more parallels can be drawn.

In enumerating higher-dimension RWs we notice the geometry of our problem; a D-dimensional generalisation of Table 3.3 has the shape of a (discretised) right hyperpyramid. The term *right* here refers to the requirement that the apex lie directly above the centre of the base, and the prefix *hyper* tells us it's generalised to any dimension. With a single spatial coordinate – and one time coordinate – we represent the number line and our construction is an isosceles triangle, with two spatial coordinates we represent a 2D lattice and get a square-based pyramid, and using a third spatial coordinate gives us what is known as a tetrahedral pyramid, the 4D equivalent, with a cube as its base. We conclude that to represent the enumeration of paths of a RW with dimensionality D we must construct a right $(D+1)$-hyperpyramid. The symmetry of a D-hyperpyramid is another facet of use to us. Understanding this fully requires a grasp of abstract geometry, but the limited scope of this report, in terms of geometry, allows us to sum up all we need by ruling that ξ_D is invariant to a reversal of sign in any and all of its spatial coordinates:

$$\xi_D(x_1,\ldots,x_D,t) = \xi_D(-x_1,\ldots,x_D,t) = \cdots = \xi_D(x_1,\ldots,-x_D,t) = \cdots = \xi_D(-x_1,\ldots,-x_D,t). \qquad (3.16)$$

Introducing a boundary condition geometrically limits the size of the hyperpyramid such that, if computed for t timesteps for the bounded $N \times \cdots \times N$ lattice where $t > N$, the hyperpyramid only extends a height of N above the base with the remaining height $t - N$ filled by a hyperrectangle. The concept of height still applies in $D > 3$ dimensions as the *right* condition means the apex and the centre of the base only differ in one of the D coordinates, the difference in which we call the height. This is exemplified for a 2D lattice in Appendix Figure A.6.

Whereas Equation (3.15) sums the three prior elements, its D-generalisation will sum the 3^D elements before it; a walker having 3^D options for the next timestep means there were 3^D options for the walker to have come from in the previous timestep. This can be seen from the kinetics explanations in Chapter 2 and is backed by our confirmation of time-reversibility above. The equation for enumerating D-dimensional paths then requires only an extension to the 1D equation. We accompany this with minimal adjustments to the notation for clarity. The 2D form of (3.15) is thus

$$\begin{aligned}
\xi_2(x,y,t+1) &= \xi_2(x-1,y+1,t) + \xi_2(x,y+1,t) + \xi_2(x+1,y+1,t) \\
&+ \xi_2(x-1,y,t) + \xi_2(x,y,t) + \xi_2(x+1,y,t) \\
&+ \xi_2(x-1,y-1,t) + \xi_2(x,y-1,t) + \xi_2(x+1,y-1,t).
\end{aligned} \qquad (3.17)$$

We also display $\xi_3(x,y,z,t)$ in Appendix Equation (A.2). Initial and boundary conditions for the 2D case (and for any D) are also the same:

$$\xi_2(0,0,0) = 1, \qquad (3.17a)$$

$$\xi_2(x,y,t) = 0 \quad \text{for} \quad \forall t < 0, \qquad (3.17b)$$

A closed-form expression for ξ can be derived using the multinomial theorem, however obtaining one for each ξ_D for $D > 1$ is difficult and there is no known generic method, and so we do not attempt it in

this report. Conversely, the simple permutations that characterise ξ_D lend themselves to very efficient programming implementations, which we demonstrate in Figure 3.4 using `MATLAB`.
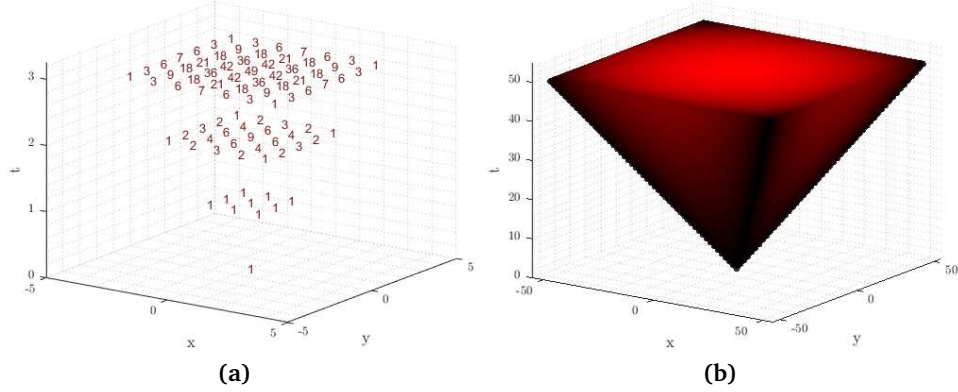

(a)   **(b)**

Figure 3.4: Path enumeration for the 2D RW for **(a)** $t \leqslant 4$, explicitly labelled, and **(b)** $t \leqslant 50$. Where coloured, the redness of node (x, y, t) is proportional to $\xi_2(x, y, t)$. Note the 4-way symmetry in all cases; for a given t all four quadrants are the same. Similar figures for confined enumeration and for $D = 1$ are shown in Appendix Figure A.6 and A.5.

We can reduce the ξ_D functions to only 2 dimensions if we 'unfurl' their pyramidal structures by iterating over values. For example unfurling ξ_2 as it appears in Figure 3.4a yields the sequence $\{1, 1, 1, 1, 1, 1, 1, 1, 1, 1, 1, 2, 3, 2, 1, \ldots, 6, 3, 1\}$. Graphing this we can directly observe some of the function's interesting properties – this can be helpful in understanding features of higher-dimension ξ_D which cannot be easily visualised for $D \geqslant 3$. There are various equivalent ways in which we can iterate over the structure due to the rotational and reflective symmetries of ξ_D. For example most 2D code implementations would do this from left to right, ascending, – or ascending, left to right – but it can be done in any manner as long as the path also obeys the pyramid's 4-way symmetry property, from Equation (3.16).
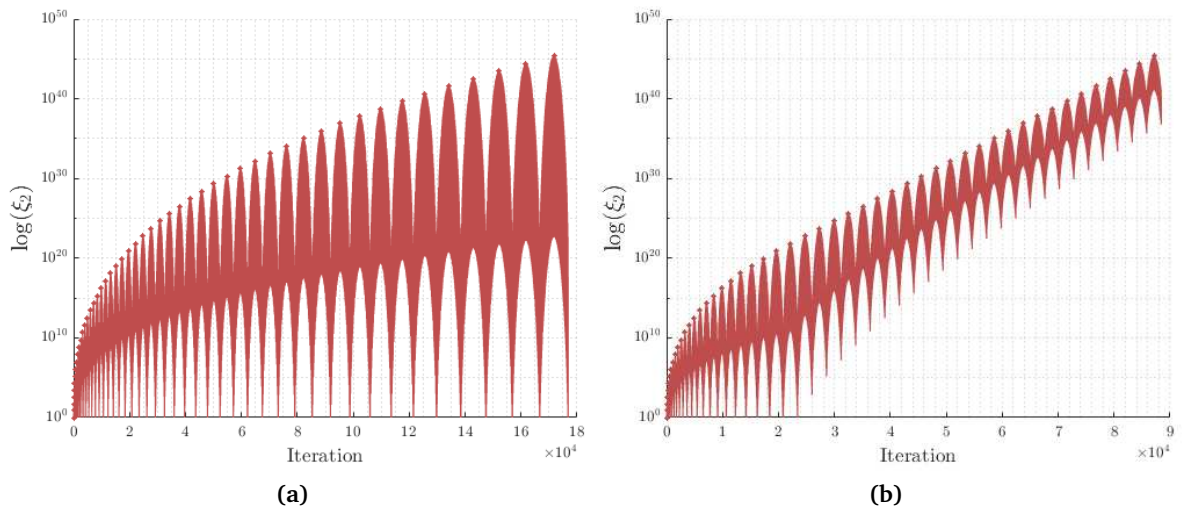

(a)   **(b)**

Figure 3.5: Plot of $\log[\xi_2(x, y, t)]$ values for $t \leqslant 50$, as in Figures 3.4 for **(a)** the unbound lattice and **(b)** a 25×25 lattice. Each spike corresponds to a layer in the pyramid and the peak its centre value. The same figures for small t and for $D = 1$ can be found in Appendix Figures A.7 and A.8 respectively.

3.2.1 Relation to ballistic walks

Walkers can be labelled *ballistic* if they exhibit behaviour in which they don't change direction or stop. Examples of this include; walkers which only change direction programmatically, as in Muñoz et al. [1996], in which case they are technically only sometimes ballistic; purely ballistic walkers that never change direction, mostly used referentially; and much more recently, ballistic walks that appear in the study of random walks in random environments [Sznitman, 2003; Guo, 2016]. Note that when talking about ballistic behaviour the number of steps and the number of timesteps are interchangeable. Up to now discussions have mainly considered symmetric walkers; the likelihood of such a D-dimensional walker exhibiting purely ballistic behaviour for t_b timesteps, with the unanimous probability condition, is

$$p_b(t_b) = \frac{p^{t_b}}{(2D)^{t_b-1}}.$$ (3.18)

We now derive (3.18) through path enumeration. Other methods exist – for example using Z-transforms or matrix manipulation [Cicuta et al., 2002] – but these fall outside the purview of this report.

First we construct another table, as before, except we now adapt our recursive path counting function ξ into a function of probabilities, henceforth denoted τ. We do this by multiplying each term associated with a movement by its likelihood of occurring:

$$\tau(x,t+1) = \frac{p}{2}\tau(x-1,t) + (1-p)\tau(x,t) + \frac{p}{2}\tau(x+1,t).$$ (3.19)

Initial conditions are akin to those for (3.15):

$$\tau(0,0) = 1,$$ (3.19a)

$$\tau(x,t) = 0 \quad \text{for} \quad \forall t < 0,$$ (3.19b)

$$\tau(x,t) = 0 \quad \text{for} \quad \forall |x| > N,$$ (3.19c)

which respectively correspond to the normalisation of τ, the non-negative time domain of τ, and the confinement of the lattice to $[-N,N]$. Now note our formal definition of ξ requires no conserved quantity; it is simply a counting function. A probabilistic analogue to ξ differs though, as probability must be conserved everywhere. This is only of concern at the boundaries, and so to match the correct rigid boundary dynamics (see Chapter 2) we fix the edges:

$$\tau(-N,t+1) = \frac{p}{2}\tau(-N+1,t) + (1-\frac{p}{2})\tau(-N,t),$$ (3.19d)

$$\tau(N,t+1) = \frac{p}{2}\tau(N-1,t) + (1-\frac{p}{2})\tau(N,t).$$ (3.19e)

-3	-2	-1	0	1	2	3
			1			
		$\frac{p}{2}$	$1-p$	$\frac{p}{2}$		
	$\left(\frac{p}{2}\right)^2$	$p(1-p)$	$\frac{p^2}{2}+(1-p)^2$	$p(1-p)$	$\left(\frac{p}{2}\right)^2$	
$\left(\frac{p}{2}\right)^3$	$\frac{3}{4}p^2(1-p)$	$\frac{15}{8}p^3-3p^2+\frac{3}{4}p$	$1-3p+\frac{9}{2}p^2-\frac{5}{2}p^3$	$\frac{15}{8}p^3-3p^2+\frac{3}{4}p$	$\frac{3}{4}p^2(1-p)$	$\left(\frac{p}{2}\right)^3$

Table 3.4: Tabular representation of $\tau(x,t)$ for $t \leqslant 3$, denoting occupational probabilities for a given x,t.

The tabular representation of τ (Table 3.4) is also a more accessible method for generating occupational probabilities and observing certain interesting dynamics, though most consider it inferior for its lack of connectivity to other fields and difficulty of analysis. For example, we can see the effects of parity without the need for simulations (see Chapter 2). Upon inspection of Table 3.4 we see the sign of leading terms in cells alternates; when x, t both have the same parity the leading term p^t is positive, and p^t is negative otherwise. This is because our starting position 0 is (effectively) even. Shifting all cells (but the headers) in Table 3.4 left by 1, we see the parities of x, t now mismatch in cells where the leading term is positive. Taking the limit $p \to 1$ then allows us to see that cells whose leading terms are negative tend to 0; this is what gives rise to the grid-like pattern showcased in Figure 2.4.

Ballistic paths are represented by both leading diagonals in Table 3.4, hence for the 1D case we find $p_{\mathrm{b}}(t_{\mathrm{b}}) = 2\left(\frac{p}{2}\right)^{t_{\mathrm{b}}}$. Conceptually then, adding D dimensions to the lattice simply adds $2D$ options to the set of possible directions (one positive and one negative for each axis), meaning the total movement probability must be now instead be evenly divided evenly into $2D$ options rather than 2. This gives us $\left(\frac{p}{2D}\right)^{t_{\mathrm{b}}}$. The standstill probability remains at $1 - p$. Finally we realise that having $2D$ possible directions also gives our D-dimensional table $2D$ diagonals, hence we can state $p_{\mathrm{b}}(t_{\mathrm{b}}) = 2D\left(\frac{p}{2D}\right)^{t_{\mathrm{b}}} = \frac{p^{t_{\mathrm{b}}}}{(2D)^{t_{\mathrm{b}}-1}}$.

Taking the case where walkers start at the centre of an $L \times L$ integer lattice, the lower bound for their escape time, i.e. time to reach the lattice boundaries, is given by the ballistic escape time. For all D the ballistic escape time is equal to the escape distance, i.e. direct distance to the boundary; for a walker starting at the centre this is $\frac{L+1}{2}$ for L odd and $\frac{L}{2} + 1$ for L even. In the 2D case for $L = 10$, $p = \frac{3}{4}$ the likelihood of a walker escaping the lattice ballistically is $p_b = 1.74 \times 10^{-4}$ – this is remarkably small and diminishes exponentially with L.

In Appendix Figure A.9 we visualise the relationship between the escape time and escape distance in isotropic walks using Monte Carlo simulations. Even plotting the first of $I = 10^5$ walkers to reach the boundary – whose paths have been found to exhibit properties vastly different to the average RW [Holcman et al., 2018] – the apparent difference between purely ballistic and isotropic walks is large and increasing rapidly with escape distance. While the number of walker instances I here cannot influence the *shape* of the gap between the ballistic and isotropic curves above, it can affect the gap's *scale* as simulating more walkers offsets their decreasing probability of a ballistic escape. This is why the curves are concurrent for $N < 15$; the probability of any one walker escaping ballistically is greater than 1, formally $I \gg p_b^{-1}$.

T his chapter serves to find the influence of different variables on the way a walk is expected to behave when it must visit every node in its domain. Common terminology for this includes the terms *completion* and *coverage*, and when considered an extension to single- or multi-target problems these tasks are often called *exhaustive searches*. The time it takes to do this, the *coverage time*, will be denoted t_C in this report. While some notable papers exist that attempt to formally find an expression for the cover time on specific topologies or by specific RW variants [Dembo et al., 2004; Abdullah, 2011; Kahn et al., 1989], this chapter will test the effects on coverage of multiple walking conditions on the reflective, confined, $\mathbb{Z}^D$ lattice by looking deeper than just the cover time.

To begin with, we reproduce the representative data provided in Table II of the famous *Universality in the lattice-covering time problem* paper by Nemirovsky et al. [1990], reviewed in greater detail in Section 1.1. This is in Appendix Table A.2 and shows largely promising results for the validity of simulations in the remainder of this chapter, despite moderately higher error margins.

We now look for a universal quantifier of coverage performance useful for comparing different RW models. A few variables are available to us here, aside from the obvious cover time figure. One standard option is the mean-square displacement (MSD) of a walker, denoted $d_{\mathrm{rms}}^2(t)$ in this paper. Formally, this is the expected squared distance travelled up to a time t, but in certain cases it has other interpretations. We use the MSD in our analysis because calculating $\langle d \rangle$ alone would yield net *displacement*, which we know is $\langle d \rangle = 0$. d_{rms}^2 is more insightful in that it captures the average distance travelled regardless of the direction of each timestep. Additional to its formal definition, we can show it to represent the expected dispersal of walkers at t by its relation to a walk's variance. Taking d_i to be the distance travelled at timestep i, we know $d_i \in \{-1, 0, 1\}$ and we define d_{rms}^2 in accordance with the above:

$$d_{\mathrm{rms}}^2(t) = \langle (d_1 + d_2 + \cdots + d_t)^2 \rangle. \tag{4.1}$$

We then split this into homogeneous and inhomogeneous products:

$$d_{\mathrm{rms}}^2(t) = \left\langle \sum_{i=1}^{t} d_i^2 + 2 \sum_{\forall i < j \leqslant t} d_i d_j \right\rangle,$$

$$= \sum_{i=1}^{t} \langle d_i^2 \rangle + 2 \sum_{\forall i < j \leqslant t} \langle d_i d_j \rangle. \tag{4.2}$$

We now realise $\langle d_i d_j \rangle = 0$ for $\forall i, j$. Physically this is due to the symmetry in movement choices and we prove this in Appendix Table A.3a. We're left with

$$d_{\mathrm{rms}}^2(t) = \sum_{i=1}^{t} \langle d_i^2 \rangle,$$

which is nothing but

$$d_{\mathrm{rms}}^2(t) = \sum_{i=1}^{t} p_d(d_i) d_i^2.$$

This is identical to the variance of the dataset $d(t) = \{d_1, d_2, \ldots, d_t\}$, a more familiar way of expressing dispersal. Formally,

$$d_{\mathrm{rms}}^2(t) = \mathrm{Var}\big[d(t)\big] = \sum_{i=1}^{t} p_d(d_i)(d_i - \mu)^2,$$

if $\mu = 0$. Indeed, this is the case for us, and so our equivalence holds.

Some terminology that surrounds this includes the term *anomalous diffusion* for processes whose d_{rms}^2 is non-linear in time, or more formally, $d_{\mathrm{rms}}^2 = \mathcal{O}(t^\gamma)$ where $\gamma \neq 1$. The process of *Brownian motion* is well-documented to have a value of $\gamma = 1$, and is often used as a benchmark; particles propagating faster than it, i.e. where $\gamma > 1$, are *superdiffusive* and those slower, i.e. $\gamma < 1$, are *subdiffusive*. Both terms are deeply rooted in the study of biochemical processes, meteorology, and countless other fields.

For the next-nearest-neighbour algorithm we need only look at the one-dimensional case; an abstraction to a higher dimension D simply requires compounding D one-dimensional RWs. For the nearest-neighbour case, though, this analysis will provide an approximate upper bound on $^{(\mathrm{NN})}d_{\mathrm{rms}}^2$ as $\langle ^{(\mathrm{NNN})}d_{\mathrm{rms}}^2 \rangle > \langle ^{(\mathrm{NN})}d_{\mathrm{rms}}^2 \rangle$ generally. In this chapter d_{rms}^2 refers to $^{(\mathrm{NNN})}d_{\mathrm{rms}}^2$ and any deviations from this will be clear from context.

In evaluating d_{rms}^2 we repeat our method exactly as before:

$$d_{\mathrm{rms}}^2(t) = \big\langle (d_1 + d_2 + \cdots + d_t)^2 \big\rangle,$$
$$= \sum_{i=1}^{t} \langle d_i^2 \rangle,$$

except now we conclude

$$d_{\mathrm{rms}}^2(t) = pt. \tag{4.3}$$

From this we can see symmetric walks set $\gamma = 1$ exactly – this hints at their well-studied approximation of Brownian motion. The mean distance travelled in t timesteps, $d_{\mathrm{rms}}(t)$, therefore scales with $\sqrt{t}$ for Brownian motion, making it generally slow for large domains. The efficacy of the d_{rms}^2 metric in measuring actual cover times is beside the point – there is also no known mathematical way to express the dependence $t_C = t_C(d_{\mathrm{rms}}^2)$, but this is enough of an indicator to show isotropic walks can be improved upon in complete coverage tasks. Moreover, the MSD evidently scales linearly with p too, for which simulatory results can be found in Appendix Figure A.13.

For the purposes of verifying (4.3) numerically and scrutinising a possible cause, Figure 4.1 is provided which shows the relationship between d_{rms}^2 and the number of boundary collisions. The co-incidence of the hike in boundary collisions and the d_{rms}^2 fluctuations suggests that the lattice's reflective boundaries strongly decelerates late-time propagation and the late-time spread of walkers. More importantly for the majority of the coverage, $t < 10^3$, the MSD is found to be linear in time as the log-log curve has an

approximately unit gradient. Specifically it is found to be 1.0613, implying a near-linear relationship $d_{\text{rms}}^2 = \mathcal{O}(t^{1.06})$. This leads to the same physical conclusion as above; after t timesteps any given walker is expected to have travelled a distance $\sqrt{t}$.
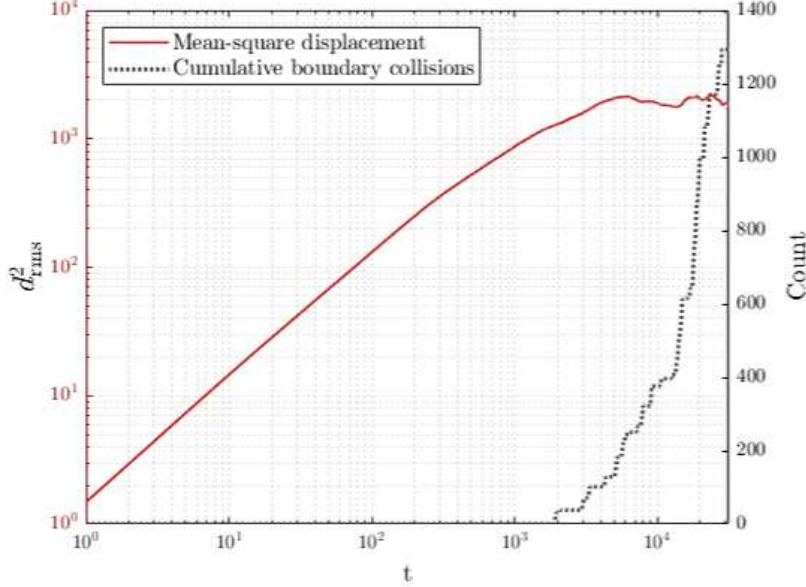

Figure 4.1: Dual-axis plot of **(left)** the log-log MSD curve and **(right)** the linear-log curve showing the number of cumulative boundary collisions. The former shows an initial monomial relation of d_{rms}^2 on t followed by a period of random fluctuations, while the latter shows how boundary collisions could influence these fluctuations. This data was averaged from $I = 30$ simulations of symmetric RW's on a 75×75 lattice where $p_1 = p_2 = \frac{3}{4}$.

Following this, we may expect increasing γ minimises t_C; to explore this further a creditable goal is to assume a different result for $\langle d_i d_j \rangle$, i.e. to discard the assumption that the walker has no bias.

4.1 Drifting model

A natural option at our disposal is to set

$$\langle d_i d_j \rangle = \beta$$

for some constant bias β. Models with such a bias are said to have a *drift* and have far-reaching applications in modelling microorganism paths in fluids [Flanders, 2019], population gene pool dynamics – aptly named *genetic drift* [Brenner and Miller, 2001], and macroeconomic trends involving long-term inflation [Nau, 2014].

We see β is the expectation of the stochastic product $d_i d_j$, so we can redefine it as the sum

$$\beta = \sum_{\forall i,j} d_i d_j p_d(d_i d_j). \tag{4.4}$$

We choose $d_i = -1$ for *left*, $d_i = +1$ for *right*, and naturally a null value for *standstill*. Let $p_d(d_i = -1) = p\delta$ for some drift δ where $0 \leqslant \delta \leqslant 1$; we then define $p_d(d_i = +1) = (1-\delta)p$ to complement this and leave $p_d(d_i = 0) = 1 - p$ unchanged. By summing all movement possibilities for any timestep i we see this conserves probability and thus is a valid paradigm to explore. Letting $\delta = 0.505$ raises the likelihood of stepping left from 50% to 50.5% of the movement probability p. Accordingly, stepping right would then be 49.5% of p and standing still would remain at $1 - p$. Extending these definitions of β, δ to an

27

arbitrary dimension D would make them vectors $\boldsymbol{\beta}, \boldsymbol{\delta} \in \mathbb{R}^D$, where each element corresponds to its own axis. Movement probabilities are then the product of probabilities for each dimension, e.g. stepping left & up in a 3D lattice has probability $p_{d_x}(d_{x,i} = -1) \times p_{d_y}(d_{y,i} = +1) \times p_{d_z}(d_{z,i} = 0) = p\delta_x \times (1 - \delta_y)p \times (1 - p)$ if we define *up* as the positive vertical direction and set a unanimous p.

Evaluating (4.4) we get

$$\beta = (2\delta - 1)^2 p^2. \tag{4.5}$$

For our method refer to Appendix Table A.3b. We immediately see this collapses to the isotropic RW at the trivial solution $p = 0$ and at $\delta = \frac{1}{2}$, corresponding to the trivial non-moving walk and to isotropic movement probabilities respectively.

In order to link δ to d_{rms}^2 we first notice that the sum through which it affects d_{rms}^2 is a sum of equal quantities, all of which are the constant $\beta = \langle d_i d_j \rangle$. We know they're equal over all $i < j \leqslant t$ from our use of the ensemble average. We next show this is a sum of $\binom{t}{2}$ quantities where $\binom{k}{s}$ is the combinatoric *choose* function, or equivalently T_{t-1} quantities where T_t is the tth triangular number. We obtain these by realising that $d_{\text{rms}}^2(t)$ is essentially a square t-nomial. To obtain the first expression $\binom{t}{2}$ we take a combinatoric approach. Consider the expanded form of $d_{\text{rms}}^2(t)$ after collecting like terms. By the multinomial theorem we know this takes the general form:

Figure 4.2: Parameter space of $\beta = (2\delta - 1)^2 p^2$. The semi-transparent grey line marks $\delta = \frac{1}{2}$.

$$d_{\text{rms}}^2(t) = \left\langle \sum_{k_1 + \cdots + k_t = 2} \frac{2!}{k_1! k_2! \cdots k_t!} \prod_{i=1}^{t} d_i^{k_i} \right\rangle.$$

It follows that the number of terms is determined by the number of solutions to the constraint $k_1 + \cdots + k_t = 2$. There are in fact an infinite number of solutions here as this represents a hyperplane in $\mathbb{R}^t$ space. For a meaningful result in the physical world, however, we only consider non-negative, integer solutions. As such we know $k_i \in \{0, 1, 2\}$ necessarily and, subsequently, there are two ways in which the above constraint could be satisfied. In one of these, $k_i = 2$ for only one of $i = 1, 2, \ldots, t$ and the remainder $k_i = 0$; we know there are precisely t of these solutions as we are effectively distributing 1 object into t boxes. In the second set of solutions, two of $i = 1, 2, \ldots, t$ set $k_i = 1$ and all other $k_i = 0$. This is essentially the number of ways of arranging 2 objects into t boxes, which we know is $\binom{t}{2}$. These correspond neatly to collecting homogeneous and inhomogeneous terms, respectively, which we did in Equation (4.2) directly without considering combinatorics. We arrive at our enumeration $\binom{t}{2}$ as we of course only consider the second scheme, in which two of $k_i = 1$ and the rest are zero, because β has no influence on the homogeneous d_i^2 terms.

The alternative approach represents the expansion of $d_{\text{rms}}^2(t)$ as a $t \times t$ table. Take the case $t = 5$ in Table 4.1. The inhomogeneous terms, once collected, populate either the upper or lower triangular sections of the table, excluding the main diagonal itself. Iterating over columns, we see this area is the sum of the first $t - 1$ natural numbers; this is precisely the $(t-1)^{\text{th}}$ triangular number T_{t-1} due to the nature of stacking objects in an alternating pattern. We can also read this relation directly from Table 4.1 if we shift each column such that we are left with a horizontal triangle with its elements in alternating align-
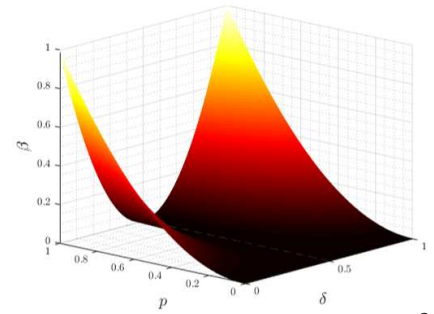
ments. The equality between our two solutions can be concisely shown by $\binom{t}{2} = \frac{t!}{2!(t-2)!} = \frac{t(t-1)}{2} = T_{t-1}$.

j $\diagdown$ i	1	2	3	4	5
1	d_1^2	$d_1 d_2$	$d_1 d_3$	$d_1 d_4$	$d_1 d_5$
2	$d_2 d_1$	d_2^2	$d_2 d_3$	$d_2 d_4$	$d_2 d_5$
3	$d_3 d_1$	$d_3 d_2$	d_3^2	$d_3 d_4$	$d_3 d_5$
4	$d_4 d_1$	$d_4 d_2$	$d_4 d_3$	d_4^2	$d_4 d_5$
5	$d_5 d_1$	$d_5 d_2$	$d_5 d_3$	$d_5 d_4$	d_5^2

Table 4.1: Tabular expansion of $d_{\text{rms}}^2(5) = \langle (d_1 + d_2 + d_3 + d_4 + d_5)^2 \rangle$.

Finally, we find

$$
\begin{aligned}
d_{\text{rms}}^2(t) &= \sum_{i=1}^{t} \langle d_i^2 \rangle + 2 \sum_{\forall i < j \leqslant t} \langle d_i d_j \rangle, \\
&= \sum_{i=1}^{t} \langle d_i^2 \rangle + t(t-1)\beta, \\
&= \beta t^2 + \left[1 - p(2\delta - 1)^2 \right] pt.
\end{aligned} \tag{4.6}
$$

Walkers whose MSD is quadratic in time are classified as ballistic in a subtly different sense of the word to that previously discussed. The above therefore tells us that a drifting walk on the $\mathbb{Z}^D$ lattice is asymptotically ballistic; $d_{\text{rms}}^2(t) \sim \beta t^2$ for our calculated β. This of course takes no consideration of reflective boundaries. We also note (4.6) is quadratic in our drift parameter δ, meaning we can maximise d_{rms}^2 by maximising or minimising δ. In line with our prior goal of increasing the time-dependence of d_{rms}^2, we may be tempted to set $\delta = 1$ (or $\delta = 0$), however we will now demonstrate that *any* $\delta \neq \frac{1}{2}$ substantially worsens coverage performance.

Although favourable in many modelling scenarios, from simulations we see drifting walkers perform poorly in completion tasks. For instance, in a 75×75 lattice, setting $\boldsymbol{\delta} = \left(\begin{smallmatrix} \delta_x \\ \delta_y \end{smallmatrix} \right) = \left(\begin{smallmatrix} 0.505 \\ 0.5 \end{smallmatrix} \right)$ results in a $160(\pm 65)\%$ jump in $^{(\text{DRF})}t_C$ compared to symmetric walkers. Again increasing δ_x to $\delta_x = 0.51$ lengthens this by $226(\pm 74)\%$ as compared with $\delta_x = 0.505$. The calculated error margins are relatively large due to limited computational resources but can be improved. These and more tabulated numerical results, including those for $D = 3$, can be found in Appendix Table A.4.

When $\beta > 0$ drifting walks theoretically undergo anomalous diffusion, albeit the range of β explored in this section affects d_{rms}^2 insignificantly, shown in Figure 4.4. A non-zero β also causes the loss of the dispersal-measuring capacity of d_{rms}^2, however where we interpret it in this and subsequent sections we read only its capacity in measuring a walk's average speed of propagation – this is still a sufficient reason to study the MSD and its variability under different walking conditions.
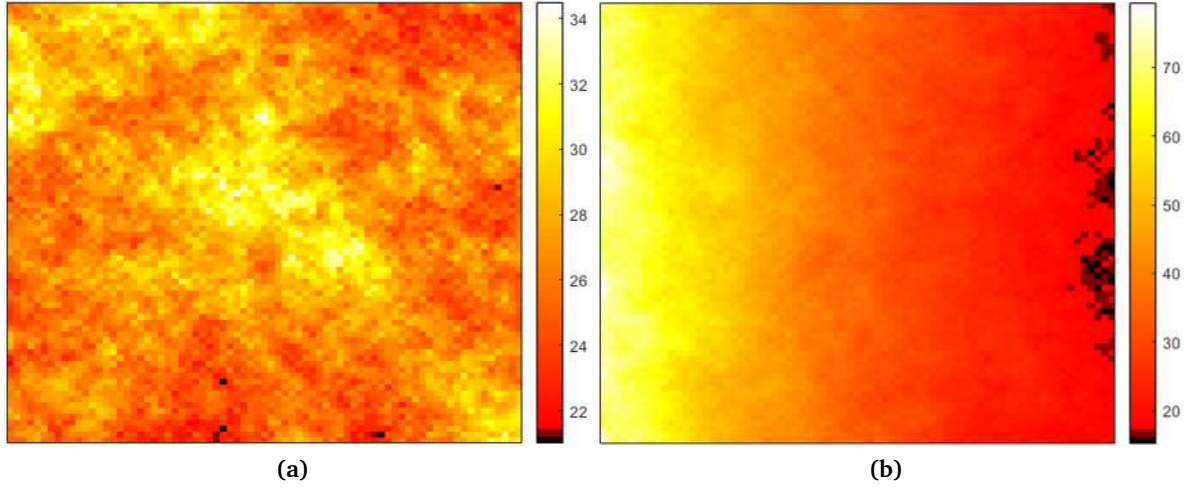
(a)   **(b)**

Figure 4.3: Heatmaps of a 75×75 simulation of the number of times each site is visited upon completion of the lattice, averaged over $I = 300$ walks where $p_1 = p_2 = \frac{3}{4}$. **(a)** $\delta_x = \frac{1}{2}$ shows an expectedly even distribution of visitations, and **(b)** $\delta_x = 0.505$ reveals a swift growth in asymmetry, even with a 1% increase in δ_x. This serves to vindicate the drifting walks' poor performance by showing what inefficient trajectories look like – this will aid in finding a more efficient coverage algorithm. Comparative heatmaps of more δ_x values can be seen in Appendix Figure A.14.

(a)   **(b)**
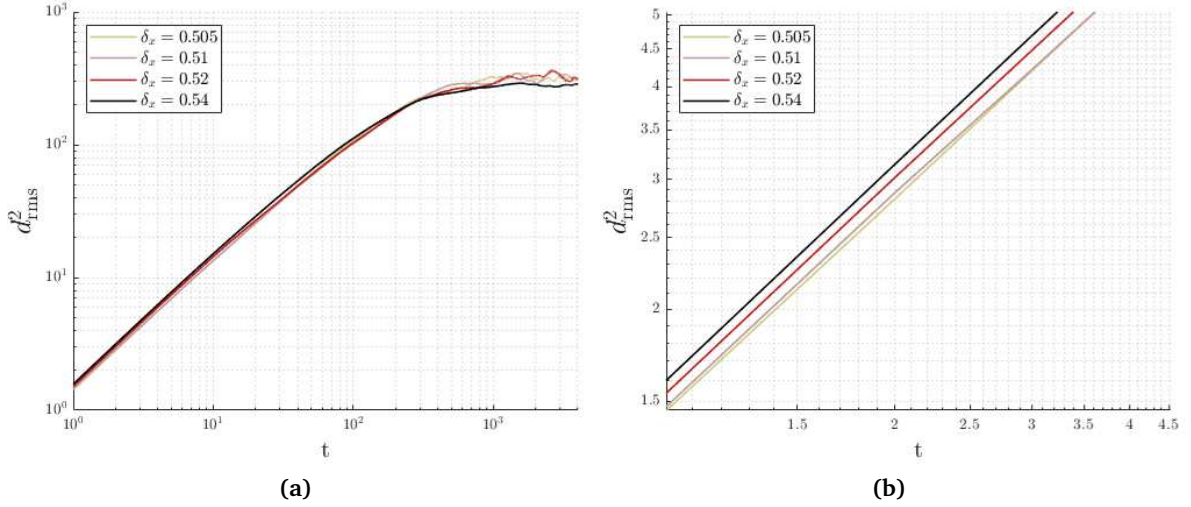
Figure 4.4: MSD data for the multiple δ_x values explored in Appendix Table A.4 and the additional $\delta_x = 0.54$, averaged over $I = 300$ and $I = 30$ trials respectively. This confirms δ is multiplicative in d_{rms}^2 as its effects are purely translational on a log-log graph. Here we set $\delta_y = \frac{1}{2}$ and $p = \frac{3}{4}$, using a 75×75 lattice.

4.2 Muñoz non-Markov model

An interesting paradigm to explore follows on from the analysis in Muñoz et al. [1996]. As briefly mentioned in Section 3.2.1, these walkers only have the choice of changing direction when in never-before-seen sites – it can therefore be said they follow non-Markovian conditions for l steps where l is the distance since the last unvisited site was occupied. Quite significantly, we set the nearest-neighbour restriction in this section to match the original work by Muñoz et al. and other work referenced later.

In this section we use $^{(\text{MNM})}t_C$ to denote the cover time for this walk.

To summarise the authors' findings, this type of walk – henceforth called the *Muñoz non-Markov walk,* or *MNM walk* for short – follows approximately normal diffusion rules initially. Then, broadly speaking, the set of visited lattice points grows radially, tending towards a rough circular shape as the walk experiences a cross-over to subdiffusive propagation. We corroborate the existence of this cluster, both for the NN and NNN case, in Appendix Figure A.15. This disparity in MSD defines two separate timescales, and the authors propose explanations for the MSD of both based on the geometry of the region of visited sites. Our analysis attempts to reproduce and confirm their results numerically, but more importantly it attempts to extend this by adjusting the author's absorbing boundary conditions.

In addition to the authors' small-t and mid-t dynamics, we expect to observe a third, large-t timescale wherein the reflectivity of the boundaries affects the time-dependence of d^2_{rms} further. Because of the author's choice of absorptive boundaries, we must consciously select different boundary conditions when constructing a simulator for coverage. Second, this means their analysis is only relevant to the extent of general movement dynamics and not with the more resource-intensive task of finding coverage dynamics. We have two sensical choices for boundary interactions; walks could either *reflect* such that only motion perpendicular to the lattice edge is reversed, or they could *scatter* such that every direction has an equal probability. The less instinctive choice of scattering was chosen as otherwise we could expect situations in which the walker ricochets indefinitely between two edges – indeed, in preliminary simulation tests this occurred surprisingly frequently and this decision was deemed necessary. This phenomenon is consequential for all walks with any degree of correlation and is discussed further in Section 4.3.

As already mentioned, we know this algorithm to not raise the time dependency of d^2_{rms} in comparison with the drifting or symmetric walk. Instead, we expect it to lead to speedier completion by other mechanisms. Namely, this walk is expected to spend significantly less time in already-visited sites. To confirm this phenomenon and compare its effects against a control we track the rate of new site visitations for a symmetric walk and an MNM walk, graphed in Figure 4.5. Prior works studying this metric denote it S_n – here we use t in place of n for time – and formally define it as the number of distinct site visits in n steps. Considerably the most common technique for its attainment is via inversion of the propagator function's Z-transform. By doing exactly this, Zumofen and Blumen [1982] have provided the asymptotic form of the symmetric S_t in 2D, adding to the 1D and 3D expressions found 20 years earlier [Vineyard, 1963].

In this report we revise the notation to $S_p(t)$ to extend the definition of S_t to allow for the inclusion of a standstill parameter. We thus attribute Zumofen's S_n (where $n \equiv t$) to a special case of $S_p(t)$, namely at $p = 1$.

We confront the findings in Zumofen and Blumen [1982] to our own new site visit data, procured from Monte Carlo `MATLAB` simulations. We bin this data into histograms, in which the height of each bar is $S_p(t)$ for that time bin. As such, the cumulative sum of our binned data follows Zumofen's S_t curve. However, we display the standalone bins in Figure 4.5, thereby allowing us to read the quotient $\frac{\text{height}}{\text{width}}$ as the local rate (i.e. for that time bin) of distinct visits. Appropriately, we select constant-width bins so that the height of each bar approximately represents the local rate $\frac{dS_t}{dt}$, only scaled by a constant. Either taking the small bin size limit or assuming a constant rate in each time bin, this quotient is $\frac{dS_t}{dt}$ exactly – without doing this, the quotient approximates $\frac{dS_t}{dt}$.

Furthermore, we propose a power law to fit the MNM $S_p(t)$ data. We regard this as only superficial, non-evidentiary fit as we lack a rigorous mathematical derivation of its general form up to some constants. As previously mentioned, Zumofen and Blumen did this using generating functions. Finding a single function to capture both the diffusive and subdiffusive modes of propagation likely merits its own chapter. The proposed limiting function has the form

$$S_p(t) = at^{-b},$$

where $a = 1.735 \times 10^5$ and $b = 0.1621$ for the $p = 1$ case studied by Muñoz et al. We also show $b \neq b(p)$ in Figure 4.6, and instead the effects of standstills on distinct site visits are only through $a = a(p)$, i.e. p is only a scaling parameter. Additional to comparing MNM new site visit data for $p = 1$ and $p = \frac{3}{4}$ in Figure 4.6, we assess separately symmetric and MNM data for $p = \frac{3}{4}$ in Appendix Figure A.16. We show p acts as a multiplicative scaling parameter in Zumofen's limit too, despite their unknowing of it.
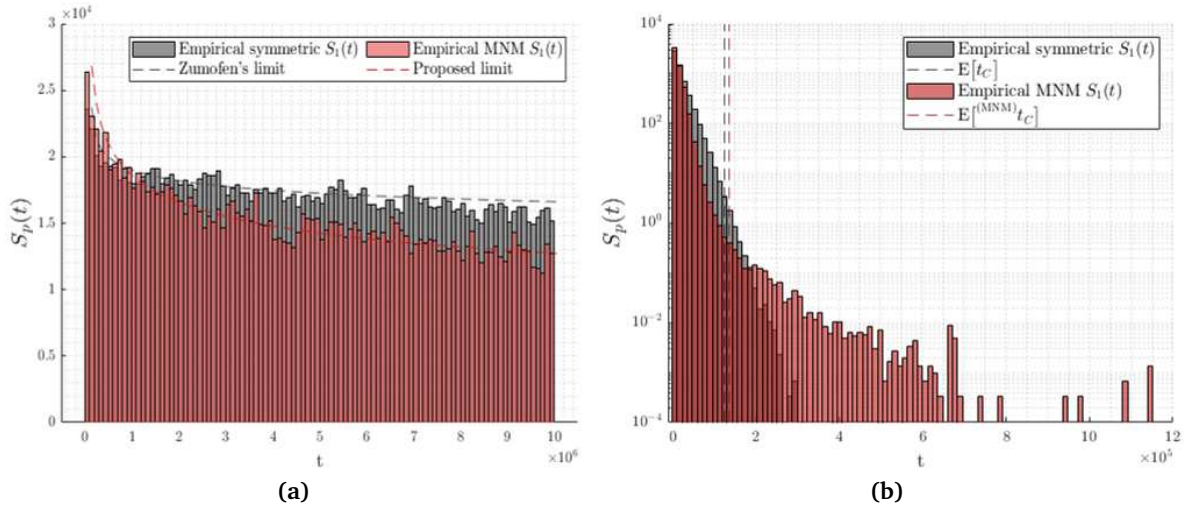
Figure 4.5: The time evolution of new site visitations for **(a)** the unbound lattice and **(b)** a 75×75 lattice, for both the Muñoz non-Markov walk and the symmetric walk. Note that the confined data is log-scaled on the vertical axis for clarity. This data was averaged from $I = 1,000$ walks where we set nearest-neighbour restrictions and $p_1 = p_2 = 1$ so as to match the original work. We use a constant bin width of **(a)** 1×10^5 and **(b)** 1.2×10^4 timesteps. This is a visualisation of 32.5GB of data, from 64 simulation hours of two simultaneous `MATLAB` instances, each calling 16 cores of *Blue Crystal phase 3*.

Looking at confined propagation, the evident long-tailedness of the histogram strongly suggests that a consequential number of data points are outliers. We suspect some degree of this is caused by the ricochet effect described earlier as our scattering boundary condition only prevents this most of the time. This is unlikely to be the sole contributor however. Extending findings by Muñoz et al., we can argue another contributing factor to the delay of lattice completion. As the central circular cluster grows – and as lattice coverage slows considerably – unvisited pockets remain at the corners of the lattice. When a walker then contacts one of these sites it almost inevitably shoots away, at most after a few timesteps. It then follows that the walker's inability to change direction in the bulk of the lattice would result in increasingly longer intervals between new site visits; the diminishing pockets are less likely to be hit by the walk's ballistic trajectory the smaller they get. This positive feedback loop is likely the main contributor to the increase of $\mathrm{E}\big[^{(\mathrm{MNM})}t_C\big]$.
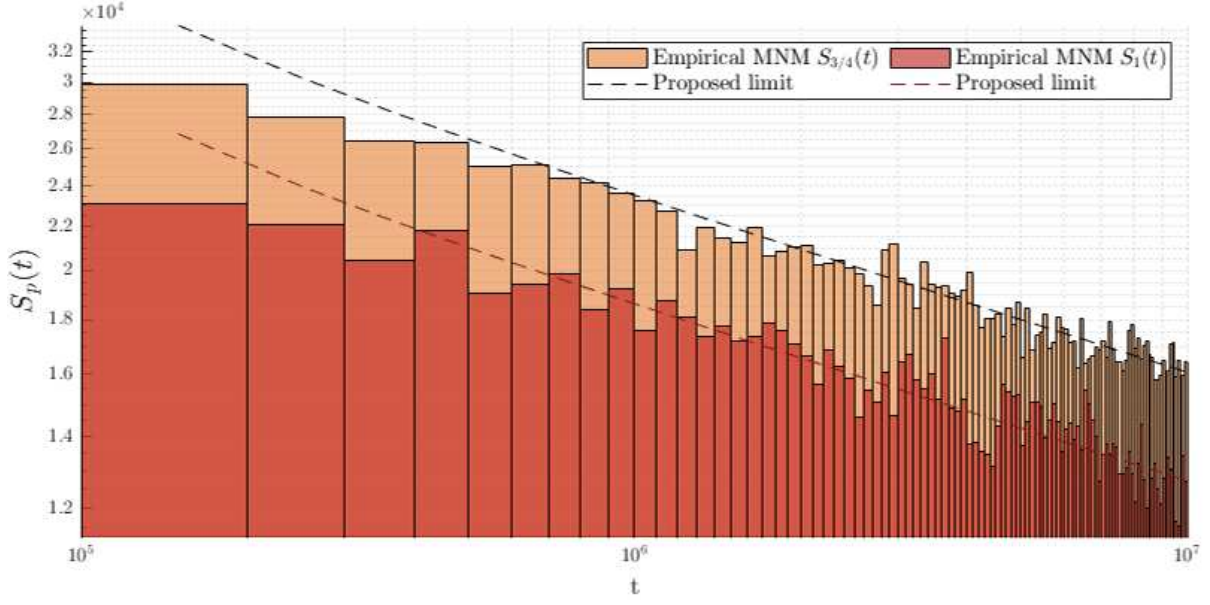
Figure 4.6: Distinct site visits (unconfined) for two p values, log-scaled on both axes to show the fit exponent b is identical. This data was averaged from $I = 300$ walks where we set nearest-neighbour restrictions, using a constant bin width of 1×10^5 timesteps. This is a visualisation of 3.3GB of data from 18 simulation hours of two simultaneous `MATLAB` instances, each calling 16 cores of *Blue Crystal phase 3*.
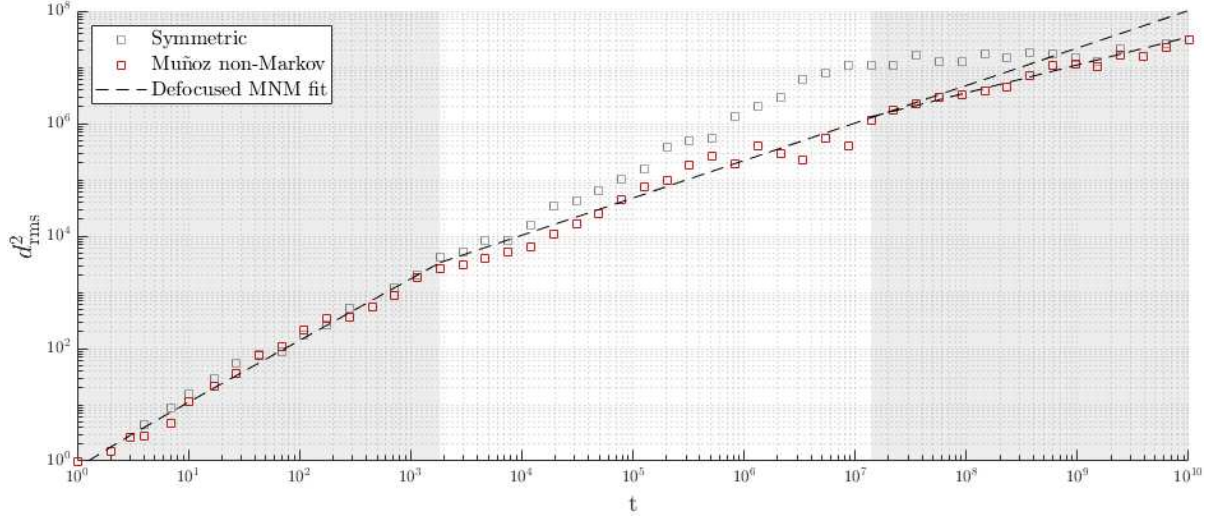
Figure 4.7: Symmetric and MNM d^2_{rms} values, divided into three time frames based on the MNM dynamics. The first displays a gradient of $\gamma = 1.0947 \pm 0.058$ and the second shows $\gamma = 0.6673 \pm 0.096$. The third period features its own fit of $\gamma = 0.4977 \pm 0.062$ as well as a continuation of the previous γ to vindicate their distinction. Due to the timescales involved, it was necessary to sample MSD values at large, logarithmically-spaced intervals rather than at every timestep for the sake of memory and computation speed. Parameter estimates are submitted in full in Appendix Table **??**, including the leading multiplicative coefficients.

In Figure 4.7 we show the same defocusing of d^2_{rms} timescales that Muñoz et al. [1996] showed. The first takes place between simulation start and $t \approx 2 \times 10^3$; this period shows a near-equivalence to Brownian propagation as the MSD values follow the power relation $d^2_{\mathrm{rms}} \propto t^\gamma$ where $\gamma = 1$ and γ is represented by the gradient in Figure 4.7. The second period follows from the last and ends at $t \approx 1.35 \times 10^7$; here the walk becomes subdiffusive, presenting a $\gamma = 0.6673$. Thus far, we have reproduced and corroborated –

with great accuracy – results from the original paper. Additionally and significantly, we also show a third timescale brought about by interactions with the boundary. The exponent here drops to $\gamma \approx \frac{1}{2}$, implying the factors affecting the prior timescale are amplified. The underlying mechanics were summarised in Muñoz et al.: "[this] supports our starting observation that the walker spends most of its time traveling across the empty central region".

4.3 Correlated model

Another RW adaptation used widely outside of mathematics is the *correlated* RW (CRW). Its applications include polymer synthesis and interaction models, in which the *entropic spring result* and other well-documented properties are derived by their similarity to paths traced by the CRW. They also have an extensive history in movement ecology [Fagan and Calabrese, 2014]. Technically just a weaker variant of the MNM regime, the correlated random walk favours, rather than guarantees, the direction it previously stepped in and only looks one timestep into the past. This should curb the supposed issue with the Muñoz non-Markov model where a positive feedback loop would arise once a large majority of the lattice has been covered. This alteration should therefore perform coverage tasks significantly better than the MNM walk; as shown in the forthcoming analysis, this is indeed the case.

A full description of the correlation mechanics used in our simulations follows. The first step a walker takes is symmetric with probability $\frac{p_d}{2}$ through each axis d – our simulations set $p_1 = p_2 = \cdots = p_D = \frac{3}{4}$. Subsequent steps are not necessarily symmetric; they instead favour the most recent direction with probability $p\alpha_d$ for correlation parameters $\alpha_1, \alpha_2, \ldots, \alpha_D$. The direction opposite to the last (through the same axis d) is then chosen with probability $(1 - \alpha_d)p$, and the standstill probability, again through this same axis, remains at $1 - p$. On collision with an edge, correlation perpendicular to that edge is reversed rather than reset – this matches the vast majority of literature concerning correlated walks.

Simulations in this section set $\alpha_1 = \cdots = \alpha_D = \alpha$. Note that this α-unanimity still allows each direction to have its own, independent α_d value of either $\frac{1}{2}$ (in case of a standstill) or α (in case of movement); they do not necessarily act in unison. For example, in a 2D lattice where $p = 0.75$ and $\alpha = 0.8$, both unanimously, walkers that move only left at $t = 1$ have a probability $p\alpha = 0.6$ of moving left (either only left, up & left, or down & left) and probability $(1 - \alpha)p = 0.15$ of moving right at $t = 2$, but due to their vertical standstill remain equally likely to move up or down as well – each with probability $\frac{p}{2} = 0.375$. The probability of movement through both dimensions is then just the product of the individual movements; moving up & left is then $0.375 \times 0.6 = 0.225$, moving down & right is $0.375 \times 0.15 = 0.05625$, etc. As evident from these figures the effects of α can be more subtle than expected.

In investigating the effects of correlation on coverage we perform a parameter sweep over α for $^{(\mathrm{COR})}t_C$. We sample cover times for increasingly small increments of α, beginning with $\Delta\alpha = 0.05$. The visualised cover time data reveals a dip in the mean cover time; this implies an α that maximally speeds up coverage. By the slope of the curve in Figure 4.8a we can infer the interval for optimal coverage to be $0.95 \leqslant \alpha \leqslant 1$. We then further discretise α to $\Delta\alpha = 0.001$ and $\Delta\alpha = 0.0001$, shown in Appendix Figure A.17 and in Figure 4.8b respectively. The data then weakly suggests that the optimal correlation is $\alpha = 0.9748$ ($\pm 0.5 \times 10^{-5}$), corresponding to a mean cover time of $9,248 \pm 65$ with the lattice configuration outlined in Figure 4.8. Note that setting $\alpha = \frac{1}{2}$ reduces the walk to behave isotropically always and choosing an $\alpha < \frac{1}{2}$ gives the walk a tendency to visit sites it has just visited by walking backwards – both
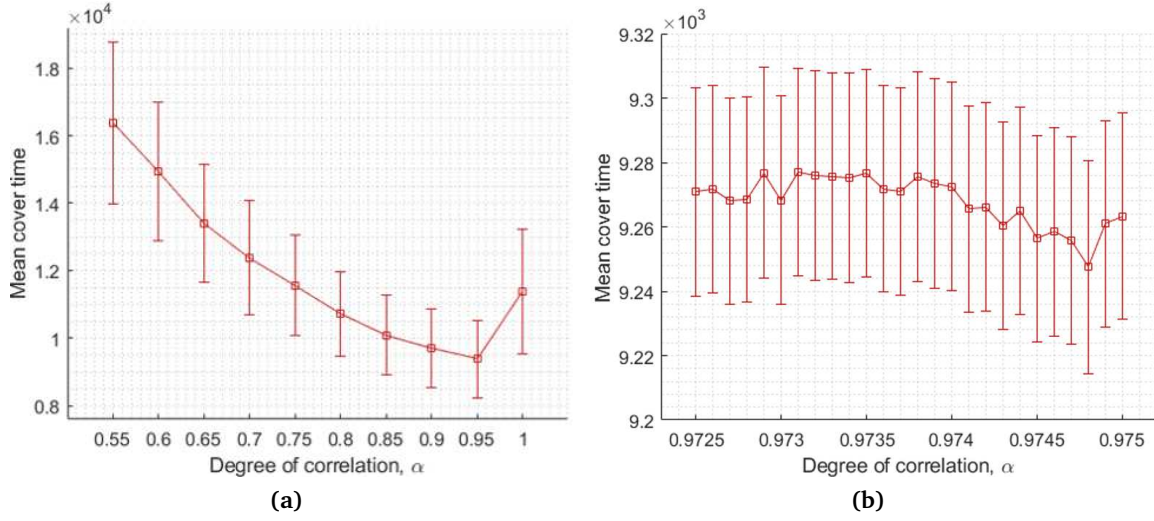
(a)   **(b)**

Figure 4.8: Mean cover times for increments of **(a)** $\Delta\alpha = 0.05$ and **(b)** $\Delta\alpha = 0.0001$, on a 75×75 lattice with $p_1 = p_2 = \frac{3}{4}$. The error bars have a length equal to one standard deviation of the samples. Due to the uncertainty in the data presented we are also limited in the certainty of our conclusion, meaning we can only say $\alpha = 0.9748$ is *most likely* to maximally speed up coverage. Number of simulations for these figures totals $15,500,000$, comprised of **(a)** $50,000$ per large increment and **(b)** $30,000$ per small increment. Total runtime is 219 hours using 8 cores of *Blue Crystal phase 3*. The same analysis for 3D correlations can be found in Appendix Figure A.18.

are known to adversely affect coverage time and hence only values of $\alpha \geqslant 0.55$ were considered.

A crucial result hidden from the above analysis is that the optimal correlation is directly affected by the lattice size. It can be reasoned that a higher degree of correlation results in longer bouts of ballistic behaviour. Specifically, for a D-dimensional lattice with unanimous p_d, α_d values, the expected ballistic distance is

$$\langle L_{\mathrm{b}}(\alpha) \rangle = p + \sum_{L_{\mathrm{b}}=2}^{\infty} p_{\mathrm{b}}(L_{\mathrm{b}}) L_{\mathrm{b}},$$

$$= p + 2D \sum_{L_{\mathrm{b}}=2}^{\infty} \left(\frac{p\alpha}{D}\right)^{L_{\mathrm{b}}} L_{\mathrm{b}}.$$

The first term p accounts for the initial step, which is symmetric in all directions and corresponds to a ballistic distance of 1. The multiplication by $2D$ accounts for ballistic behaviour in any direction in the lattice (barring a standstill), and the summation accounts for all ballistic distances after the first step, where the $p_{\mathrm{b}}(L_{\mathrm{b}})$ derived in Section 3.2.1 is a special case of the above in which $\alpha = \frac{1}{2}$. Since $\langle L_b(\alpha) \rangle$ is a monotonically increasing function of α, it follows that strengthening the correlation would result in longer ballistic runs. In smaller lattices the likelihood of walks ricocheting between walls will increase with $\langle L_b \rangle$ too, which would needlessly cover the same sites and delay lattice completion. In the limit $\alpha \to 1$ observed trajectories will approach purely ballistic ones, for which we know coverage is inefficient. For this reason weaker correlations are preferred for smaller lattices. Conversely, larger lattices should favour a larger $\langle L_b \rangle$; when longer ballistic runs arise – and the lattice is large enough to accommodate for them – the walk will spend more time exploring new areas. This is the fundamental idea behind superdiffusive processes, which propagate through a medium faster than random Brownian motion – a precondition for speedier coverage.

CONCLUSION

Through this report, we wish to illustrate the rich statistical properties that arise from some of the simplest, most elementary processes; the discrete random walk and its basic variants. Split into two chapters, our research considers the behaviour random walks exhibit when propagating freely, whether confined or unconfined, and when tasked with the coverage of a domain. We supplement this with a preliminary chapter on the historical and literary context of the random walk, and, wherever possible, provide explanations through simple and informative visualisations. In our analysis we have also uniquely included a standstill probability, a relatively recent concept with a sparse formal understanding.

After contextualising our research, in the second chapter we introduced concepts and notation crucial to the ensuing analyses. We described the rules governing random walk mechanics and alluded to the derivation of the occupational probability function P_{n_0} for up to two dimensions, although we provided the generalised formula too. We only included an allusion to this as it belongs, in its full length, to Giuggioli [pp] in his yet-unpublished work on discrete propagation. Additionally, our main concern is with the utility of P_{n_0} and so we count its derivation superfluous. Despite the straightforward explanations to which random walks lend themselves, the dynamics implied by their propagator function are not immediately obvious, nor is it obvious how their dynamics lead to the formulation of their propagator function. To overcome this and confirm their equivalence we confronted a Monte Carlo implementation of the symmetric walk with the evaluation of P_{n_0}, on the same lattice and in dimensions $D \leqslant 3$. The general impact of parity issues were also briefly discussed here.

The third chapter is the first of our original research and is partitioned into two sections. The first section tackled the historically elusive task of fully computing the first-passage time distribution. It also demonstrated some relational properties of this distribution. This has seldom been attempted in the literature on discrete RWs; its analytic expression has been found only for the 1D case, and higher-dimension analyses usually obtain only the analytic distribution which some of its moments define [Bénichou et al., 2005]. The actual FPT distribution, however, is not guaranteed to be uniquely determined by this due to the infinite interval on which the FPT operates, and extra conditions (such as Carleman's condition) are necessary to make it so. What we have provided is an alternate method for computing this distribution, by means of numerically inverting the occupational probability's generating

function. This is a novel approach which utilises a relatively new and unknown inversion algorithm. Accordingly, we took particular caution in qualifying the accuracy of our results, despite the authors' esteemed reputation.

In the second section, through basic recurrence relations we presented the enumeration of RW paths on lattices of dimensionality $D \leqslant 3$, although, again, the geometric and computational explanations provided are sufficiently generalised for any dimension. We studied the relation our problem exhibits to the trinomial expansion, arising specifically from our inclusion of a standstill. This section also derived a formula for the probability of a ballistic trajectory occurring within a given length of time.

The fourth and final chapter investigated how certain RW variants perform coverage tasks. Naturally, this was a largely exploratory analysis. In it, we not only looked at the coverage time t_C itself, but also the manner of propagation – as such, we found the d_{rms}^2 metric an incredibly useful tool. This chapter confirmed results for the propagation of drifting walkers formally and through simulations, pertaining to the exact influence of the drift parameter δ on the MSD. Next, we reproduced and extended the analysis on the long range non-Markov model first studied by Muñoz et al. [1996]. In doing so, we find a third timescale in which boundary conditions impact propagation. Finally, we considered the more classic correlated walk model whose correlation parameter α effectively weakened the non-Markovian effects seen in the MNM walk. Here we found an optimal α for minimising $^{(\mathrm{COR})}t_C$, though the stochastic nature of RWs means our evidence only weakly supports our conclusion. We note that a large amount of data was lost relating to this analysis as OneDrive folders created after a certain time were lost. This has meant our process of refining the interval of α for minimal coverage in 3D could not be provided here. It also meant graphs made prior to the loss could not be redrawn to match the style of rest of the report, once this style was finalised.

5.1 Improvements

We suggest that researchers looking to continue this research spend a significant amount of resources on code optimisation. Sluggish code heavily influenced our rate of work and we believe it is a key factor in the quality of research we output. The 2D occupational probability, in a lattice of size $N \times M$, requires a summation of a summation; if done using for-loops, their time complexity is $\mathcal{O}(NM)$. In general, the occupational probability calculation for a rectangular lattice of size $N_1 \times N_2 \times \cdots \times N_D$ has time complexity $\mathcal{O}(N_1 N_2 \cdots N_D)$. The same complexity is also seen in our implementation of Whitt's inverse Z-transform for FPPs, though this is likely unavoidable. A similarly adverse complexity of $\mathcal{O}(t^2)$ is exhibited by our for-loop MSD calculator, as every timestep must be compared against every other.

To make these more efficient, we ideally exploit our chosen programming language's strengths; this report is almost completely built on MATLAB, hence our ideal solution vectorises these operations. For this, a large volatile memory is imperative; even with access to 4GB of RAM, on top of *Blue Crystal phase 3* access, this was still insufficient to fully vectorise MSD calculations for data storing over 1×10^5 timesteps. Second, this requires a meticulous conversion of every variable to matrix form and every operation to a matrix-optimised form, with rigorous testing. This is not always straightforward, though with improved time management and programming skills it is certainly possible.

Additionally, time constraints have meant that a lot of interesting research could not be addressed in this report. Some inexhaustive examples include:

- How does the sequence of central $\xi_D(x,t)$ values, $a_D(t)$, vary with t for $D > 1$? How does it vary with D? Leonhard Euler studied the $D = 1$ case, dedicating the 20-page article *Observationes analyticae* to $a_1(t)$ and related series, and found a summation formula to generate them among other notable results. Our analysis ends prematurely, and an extension of Euler's work on the central ξ_D values could be interesting.

- How does the NNN Muñoz non-Markov walk compare with its NN counterpart? Our section on this set NN restrictions so we could incorporate established results in our analysis, however an investigation on the difference between the two would be beneficial. The same can be asked of any of the RW variants we considered.

- How does the Muñoz non-Markov walk's new visit rate vary? Our analysis includes a simple power law fit, however a more mathematically rigorous and evidence-based analysis would yield much more meaningful results.

- How does the distribution of $^{(\mathrm{MNM})}t_C$ vary with lattice size? If this relationship was found to be exponential, it could provide substantial evidence for our hypothesis on the factors lengthening mean coverage.

- How does correlation strength α affect lattice exploration? Again, our work on $\langle L_\mathrm{b} \rangle$ had to be cut short here but a deeper analysis, e.g. one that looks at $S_p(t)$, could have interesting consequences for the numerous applications we discuss.

Abdullah, M. (2011). The cover time of random walks on graphs (doctoral dissertation). *Cornell University Library*.

Adal, K. M., Samir, B. B., and Ali, N. B. Z. (2010). Biased random walk based routing for mobile ad-hoc networks. pages 1 – 6.

Andrews, G. E. (1990). Euler's "exemplum memorabile inductionis fallacis" and q-trinomial coefficients. *Journal of the American Mathematical Society*, 3:653 —- 669.

Bachelier, L. (1900). La théorie de la spéculation. *Annales scientifiques de l'École Normale Supérieure*, 17:21 – 86.

Brenner, S. and Miller, J. H. (2001). *Encyclopedia of Genetics*. Academic Press.

Bénichou, O. and Condamin, S. (2006). Exact expressions of mean first-passage times and splitting probabilities for random walks in bounded rectangular domains. *Journal of Chemical Physics*, 124(20):206103.

Bénichou, O., Condamin, S., and Moreau, M. (2005). Random walks and brownian motion: A method of computation for first-passage times and related quantities in confined geometries. *Physical Review E*, 75:021111.

Bénichou, O., Loverdo, C., Moreau, M., and Voituriez, R. (2011). Intermittent search strategies. *Reviews of Modern Physics*, 83:82 – 127.

Chupeau, M., Bénichou, O., and Voituriez, R. (2015). Cover times of random searches. *Nature Physics*, 11:844 – 847.

Cicuta, G. M., Contedini, M., and Molinari, L. (2002). Enumeration of simple random walks and tridiagonal matrices. *Journal of Physics A: Mathematical and General*, 35:1125 —- 1146.

Dembo, A., Peres, Y., Rosen, J., and Zeitouni, O. (2004). Cover times for brownian motion and random walks in two dimensions. *Annals of Mathematics*, 4:433 – 464.

Ehrhardt, G. (2013). The not-so-random drunkard's walk. *Journal of Statistics Education*, 21.

Einstein, A. (1905). Über die von der molekularkinetischen theorie der wärme geforderte bewegung von in ruhenden flüssigkeiten suspendierten teilchen. *Annalen der Physik*, 322.

Fagan, W. F. and Calabrese, J. M. (2014). The bulletin of the ecological society of america. *Oecologia*, 95:204 —- 206.

Fateman, R. J. and Kahan, W. (2000). Improving exact integrals from symbolic algebra systems.

Flanders, W. (2019). Biased random walk. *Flander's Health Blog*.

Flygare, M. (2012). Some properties of infinite series. *Bachelor's Thesis, Karlstad University Department of Mathematics*.

Franklin, A. (2018). Analytics of single- and multi-target problems for bounded random walks. *Master's Thesis, University of Bristol Department of Engineering Mathematics*.

Galceran, E. and Carreras, M. (2013). A survey on coverage path planning for robotics. *Robotics and Autonomous Systems*, 61:1258 – 1276.

Giuggioli, L. (p.p.). Exact propagators for conned discrete random walks in any dimension.

Grebenkov, D. S., Metzler, R., and Oshanin, G. (2018). Strong defocusing of molecular reaction times results from an interplay of geometry and reaction control. *Communications Chemistry*, 1(96).

Guo, X. (2016). Einstein relation for random walks in random environment. *The Annals of Probability*, 44:324 – 359.

Holcman, D., Basnayake, K., Guerrier, C., and Schuss, Z. (2018). Asymptotics of extreme statistics of escape time in 1,2 and 3-dimensional diffusions. *Journal of Nonlinear Science*, 29:461 —- 499.

Kahn, J. D., Linial, N., Nisan, N., and Saks, M. E. (1989). Cover times for brownian motion and random walks in two dimensions. *Journal of Theoretical Probability*, 2:121 – 128.

Krummel, M. F., Bartumeus, F., and Gérard, A. (2016). T cell migration, search strategies and mechanisms. *Nature Reviews Immunology*, 16:193 – 201.

Lin, J., Gupta, P., Goel, A., Sharma, A., Zadeh, R., and Wang, D. (2013). Wtf: the who-to-follow service at twitter. pages 505 – 514.

Lugo, M. (2007). Variations on the drunken-bird theorem, and real-world sightings. *God Plays Dice*.

Muñoz, M. A., Molinàs-Mata, P., Martínez, D. O., and Barabási, A.-L. (1996). Ballistic random walker. *Physical Review E*, 54:968 – 971.

Nagar, A. and Pradhan, P. (2003). First passage time distribution in random walks with absorbing boundaries. *Physica A: Statistical Mechanics and its Applications*, 3220:141 – 148.

Nau, R. (2014). Notes on the random walk model.

Nemirovsky, A. M. and Coutinho-Filho, M. D. (1991). Lattice covering time in d dimensions: theory and mean field approximation. *Physica A*, 177:233 – 240.

Nemirovsky, A. M., Mártin, H. O., and Coutinho-Filho, M. D. (1990). Universality in the lattice-covering time problem. *Physical Review A*, 41:761 – 767.

Pearson, K. (1905). The problem of the random walk. *Nature*, 72:294.

Sznitman, A.-S. (2003). On new examples of ballistic random walks in random environment. *The Annals of Probability*, 1:285 – 322.

Vineyard, G. H. (1963). The number of distinct sites visited in a random walk on a lattice. *Journal of Mathematical Physics*, 4:1191 – 1193.

Viswanathan, G. M., Raposo, E., and da Luz, M. G. E. (2008). Lévy flights and superdiffusion in the context of biological encounters and random searches. *Physics of Life Reviews*, 5:133 – 150.

Whitt, W., Choudhury, G. L., and Abate, J. (2000). An introduction to numerical transform inversion and its application to probability models. *Computational Probability*, 24:257 —- 323.

Xia, F., Liu, J., Nie, H., Fu, Y., Wan, L., and Kong, X. (2019). Random walks: A review of algorithms and applications. *Transactions on Emerging Topics in Computational Intelligence*, pages 1 – 13.

Yokoi, C. S., Hernández-Machado, A., and Ramírez-Piscina, L. (1990). Some exact results for the lattice covering time problem. *Physics Letters A*, 145:82 – 86.

Yueh, W.-C. (2005). Eigenvalues of several tridiagonal matrices. *Applied Mathematics E-Notes*, 5:66 – 74.

Zumofen, G. and Blumen, A. (1982). Energy transfer as a random walk. ii. two dimensional regular lattices. *Journal of Chemical Physics*, 76:3713 – 3731.
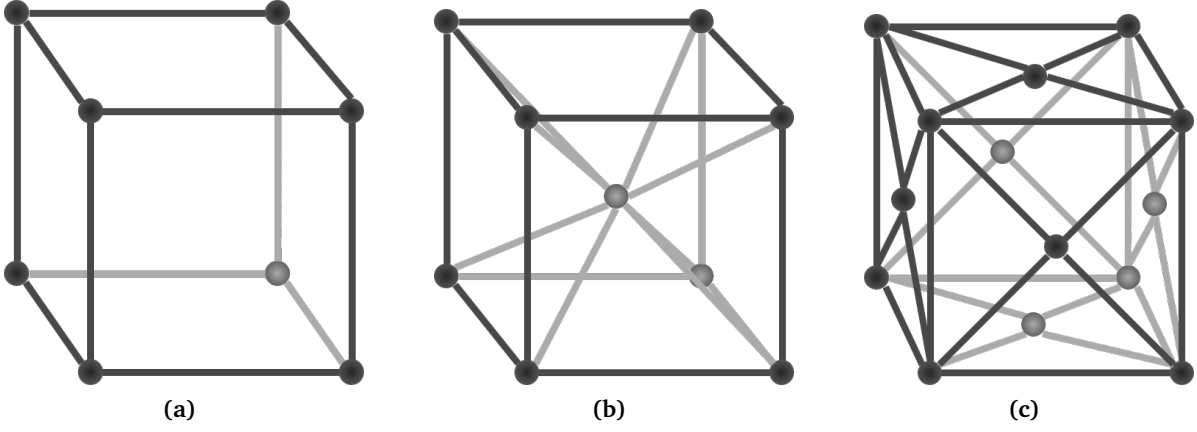
Figure A.1: The **(a)** primitive cubic, **(b)** body-centred cubic, and **(c)** face-centred cubic cell; the three types of 3D Bravais lattice structures commonly studied in related precedent research.

$$P_{\boldsymbol{n}_0}(\boldsymbol{N},\boldsymbol{n},p,t) = \frac{1}{\prod_{d=1}^{D} N_d} \sum_{k_1=1}^{N_1} \sum_{k_2=1}^{N_2} \cdots \sum_{k_D=1}^{N_D} \prod_{d=1}^{D} \alpha_{k_d} \cos\left[(2n_d-1)\frac{(k_d-1)\pi}{2N_d}\right] \cos\left[(2n_{0,d}-1)\frac{(k_d-1)\pi}{2N_d}\right] \lambda_{k_d}^t.$$

(A.1)

Appendix Equation A.1: Generalised occupational probability function.

(a)   **(b)**
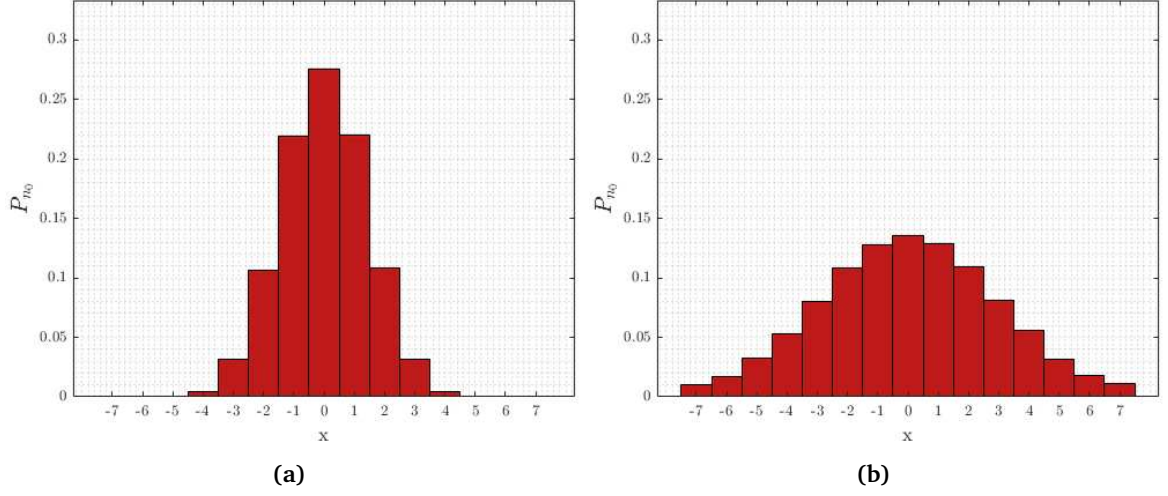
Figure A.2: Occupational probabilities for the 1D interval $[-7,7]$ at timesteps **(a)** $t = 5$ and **(b)** $t = 18$. Here $p = \frac{3}{4}$ and walkers all start at the origin..

$$
\begin{aligned}
\xi_3(x,y,z,t+1) \;=\; & \xi_3(x-1,y+1,z-1,t) + \xi_3(x,y+1,z-1,t) + \xi_3(x+1,y+1,z-1,t) \\
& + \xi_3(x-1,y,z-1,t) \;\;\; + \xi_3(x,y,z-1,t) \;\;\;\;\; + \xi_3(x+1,y,z-1,t) \\
& + \xi_3(x-1,y-1,z-1,t) + \xi_3(x,y-1,z-1,t) + \xi_3(x+1,y-1,z-1,t) \\
& + \xi_3(x-1,y+1,z,t) \;\;\; + \xi_3(x,y+1,z,t) \;\;\;\;\; + \xi_3(x+1,y+1,z,t) \\
& + \xi_3(x-1,y,z,t) \;\;\;\;\;\; + \xi_3(x,y,z,t) \;\;\;\;\;\;\;\; + \xi_3(x+1,y,z,t) \\
& + \xi_3(x-1,y-1,z,t) \;\;\; + \xi_3(x,y-1,z,t) \;\;\;\;\; + \xi_3(x+1,y-1,z,t) \\
& + \xi_3(x-1,y+1,z+1,t) + \xi_3(x,y+1,z+1,t) + \xi_3(x+1,y+1,z+1,t) \\
& + \xi_3(x-1,y,z+1,t) \;\;\; + \xi_3(x,y,z+1,t) \;\;\;\;\; + \xi_3(x+1,y,z+1,t) \\
& + \xi_3(x-1,y-1,z+1,t) + \xi_3(x,y-1,z+1,t) + \xi_3(x+1,y-1,z+1,t)
\end{aligned}
\tag{A.2}
$$

Appendix Equation A.2: The recursive path enumeration formula for $\mathbb{Z}^3$. Initial and boundary conditions are conceptually identical to the 1D and 2D cases; at $t = 0$ all $\xi_3(x,y,z,0) = 0$ except $\xi_3(0,0,0,0) = 1$, all negative-time-valued ξ_3 are null, and $\xi_3(x,y,z,t) = 0$ for $\forall |x|,|y|,|z| > N$ if the lattice is a cube whose sides span $[-N,N]$.

$$
\mathscr{P}_{\boldsymbol{n}_0}(\boldsymbol{N},\boldsymbol{n},p,z) = \frac{1}{\prod_{d=1}^{D} N_d} \sum_{k_1=1}^{N_1} \sum_{k_2=1}^{N_2} \cdots \sum_{k_D=1}^{N_D} \frac{\prod_{d=1}^{D} \alpha_{k_d} \cos\left[(2n_d - 1)\frac{(k_d-1)\pi}{2N_d}\right] \cos\left[(2n_{0,d} - 1)\frac{(k_d-1)\pi}{2N_d}\right]}{1 - z\prod_{d=1}^{D} \lambda_{k_d}}.
\tag{A.3}
$$

Appendix Equation A.3: Z-transform of the symmetric D-dimensional occupational probability. Here the starting node is $\boldsymbol{n}_0 = [n_{0,1} \;\; n_{0,2} \;\; \cdots \;\; n_{0,D}]$, the lattice size is given by $\boldsymbol{N} = [N_1 \;\; N_2 \;\; \cdots \;\; N_D]$, and the target node is $\boldsymbol{n} = [n_1 \;\; n_2 \;\; \cdots \;\; n_D]$.

(a)		**(b)**	
Target node n	Gradient/decay rate	Target node $\boldsymbol{n}$	Gradient/decay rate
$n_0 + 1$	-2.1892×10^{-8}	(N, m_0, s_0)	-1.7584×10^{-9}
$n_0 + 2$	-2.1404×10^{-8}	(N, M, s_0)	-1.4437×10^{-9}
$n_0 + 3$	-1.8742×10^{-8}	(N, M, S)	-1.1653×10^{-9}

Table A.1: Numeric gradients values for **(a)** three nearby endpoints on the $[1,50]$ number line and **(b)** three far-apart endpoints on the $50 \times 50 \times 50$ cubic lattice. In these, $\boldsymbol{n}_0$ is the centre of the lattice and $p = \frac{3}{4}$ unanimously.
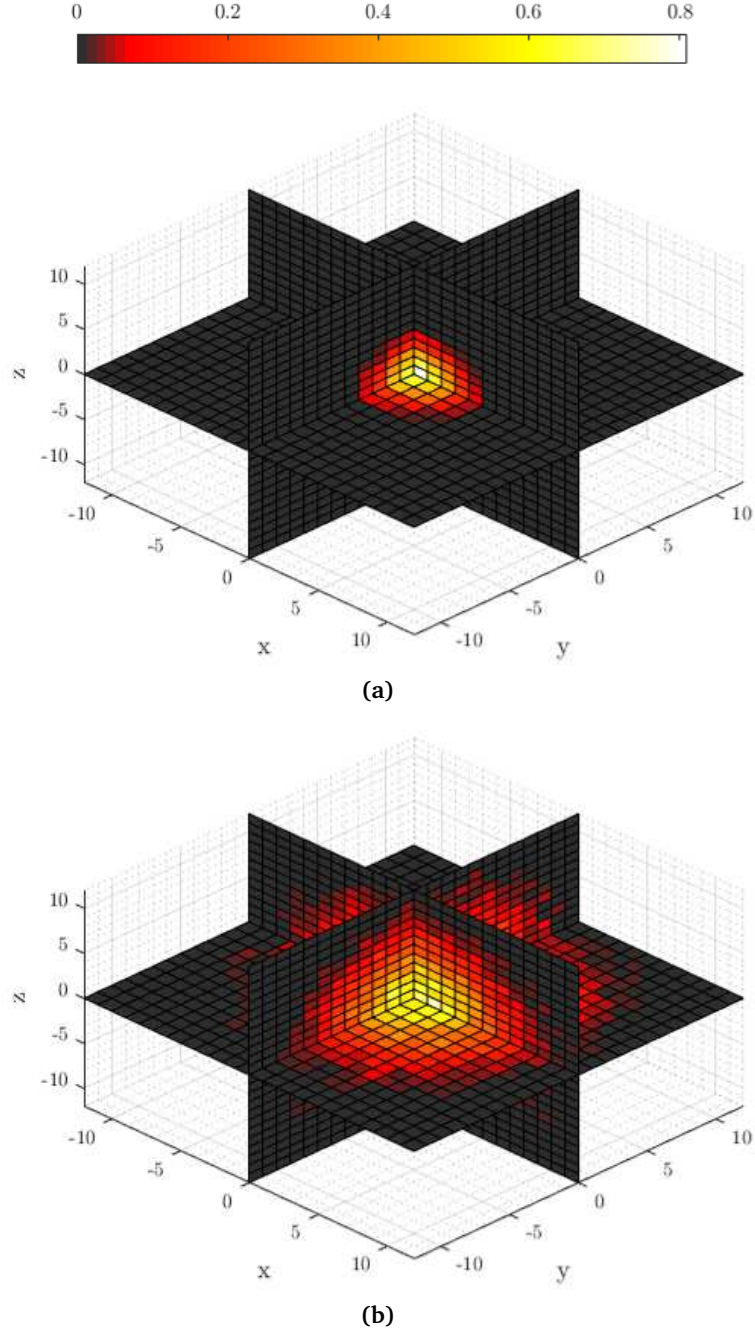
(a)

(b)

Figure A.3: Occupational probabilities for a $25 \times 25 \times 25$ lattice at timesteps **(a)** $t = 5$ and **(b)** $t = 18$, represented by the colour of the node. Here $p_1 = p_2 = \frac{3}{4}$, walkers all start at the centre node $(0,0)$, and slices through the cube were taken through the origin.
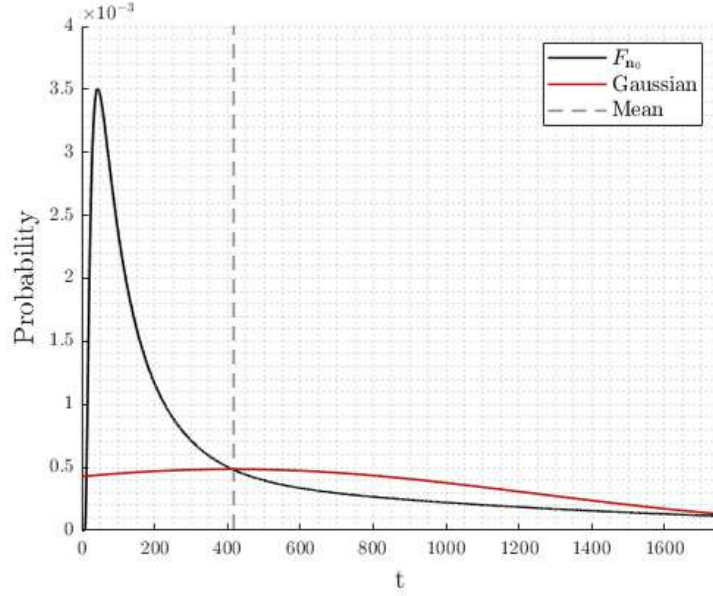
Figure A.4: Visual interpretation of our distribution's $\tilde{\mu}_3, \tilde{\mu}_4$ moments. From this we clearly see a positive skew; not only from the right tailedness but also from the inequality mean > median, where the median is the peak. We also confirm our sub-Gaussian kurtosis by overlaying our distribution with a Gaussian of the same mean and variance. The FPP tails are dominated by the Gaussian's and the slope is (much) steeper around the mean – these are typical of a platykurtic distribution. For this we set $p_1 = p_2 = \frac{3}{4}$ in a 50×50 lattice, with endpoints $\boldsymbol{n}_0$ at the centre and $\boldsymbol{n}$ at $\boldsymbol{n} = [30\ 30]$.

| N	Cover time, $n_0 = 1$	$N(N-1)$	Cover time, $n_0 = \frac{N}{2}$	$\frac{N(5N-6)}{4}$
4	13.1 ± 3.04	12	15.1 ± 3.14	14
6	31.4 ± 6.47	30	36.9 ± 4.98	36
8	56.8 ± 10.5	56	67.9 ± 6.71	68
10	91.8 ± 15.8	90	111 ± 8.74	110
30	874 ± 94.9	870	$1,078 \pm 27.2$	1,080
60	$3,487 \pm 292$	3,540	$4,443 \pm 54.6$	4,410
120	$(1.45 \pm 0.09) \times 10^4$	1.428×10^4	$(1.78 \pm 0.09) \times 10^4$	1.782×10^4
250	$(6.17 \pm 0.3) \times 10^4$	6.225×10^4	$(7.72 \pm 0.3) \times 10^4$	7.775×10^4
500	$(2.50 \pm 0.09) \times 10^5$	2.495×10^5	$(3.13 \pm 0.09) \times 10^5$	3.1175×10^5
1,000	$(1.00 \pm 0.03) \times 10^6$	0.999×10^6	$(1.23 \pm 0.03) \times 10^6$	1.2485×10^6

Table A.2: Reproduction of Table II from Nemirovsky et al. [1990]. All values are to 3 s.f., the errors are one standard deviation of the collected samples, and $I = 30,000$ samples were collected per data point. We set $p = 1$ to match the original work's dynamics and starting nodes are conveyed in the headers.
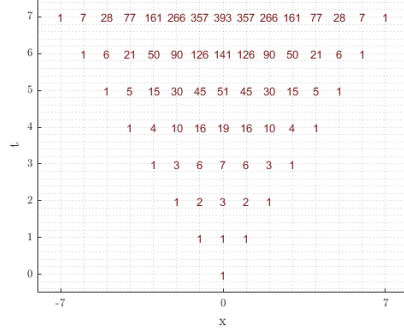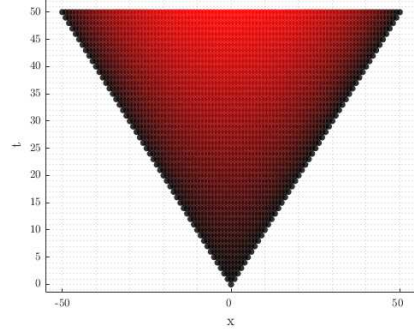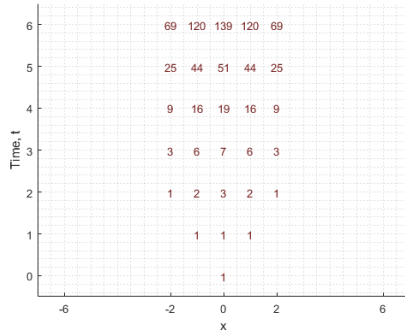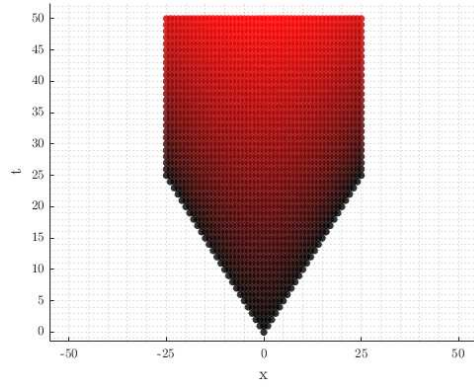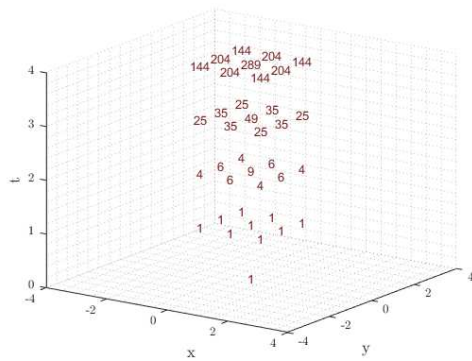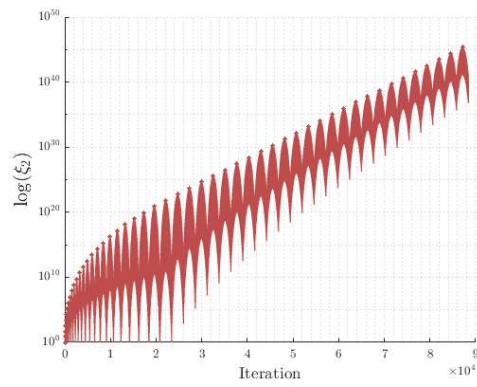
Figure A.5: Path enumeration on the number line for **(a)** $t \leqslant 7$, explicitly labelled, **(b)** $t \leqslant 50$, **(c)** $t \leqslant 6$, explicitly labelled and bound to $[-2, 2]$, and **(d)** $t \leqslant 50$, bound to $[-25, 25]$. Where coloured, the redness of (x, t) is proportional to $\xi(x, t)$.

Figure A.6: 2D path enumeration for **(a)** $t \leqslant 5$, explicitly labelled and bound to a 3×3 lattice, and **(b)** $t \leqslant 50$ when bound to a 25×25 lattice. Where coloured, the redness of node (x, y, t) is proportional to $\xi_2(x, y, t)$.

(a) **(b)**
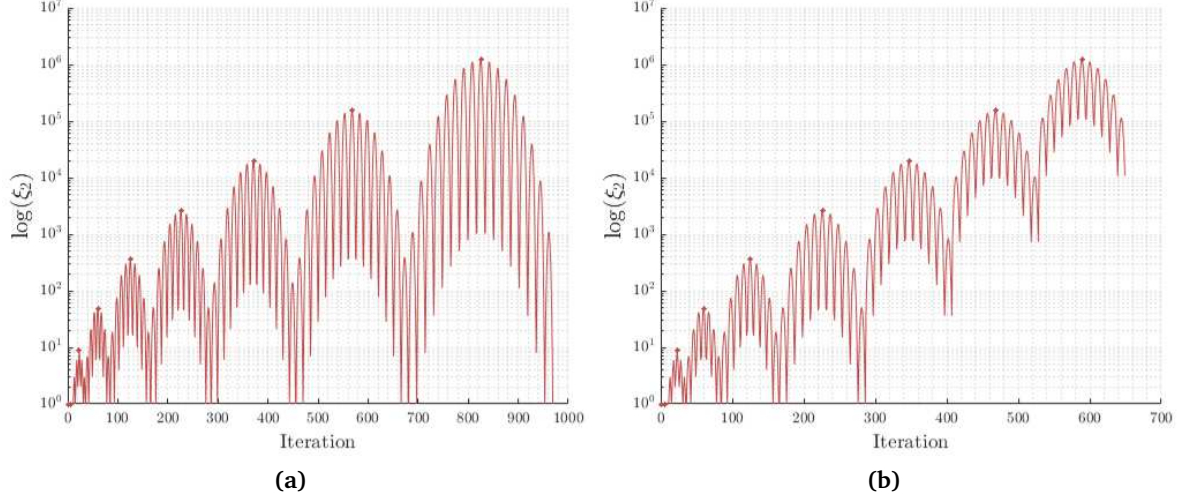
Figure A.7: $\log\left[\xi_2(x,y,t)\right]$ for $t \leqslant 8$ on **(a)** the unbound lattice and **(b)** a 5×5 lattice. Compared to maintext Figure 3.5, downscaling our analysis allows us to more clearly see the size of each layer being restricted once t surpasses the lattice size constraint (5 in this case).
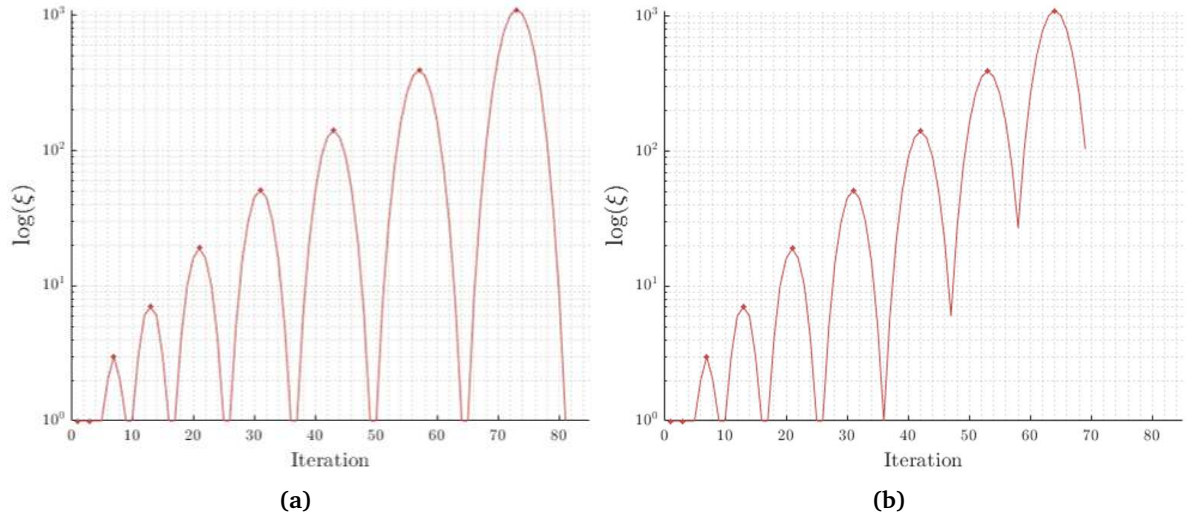

(a) **(b)**

Figure A.8: $\log\left[\xi(x,t)\right]$ for $t \leqslant 8$ on **(a)** the unbound lattice and **(b)** on a 5×5 lattice.

46
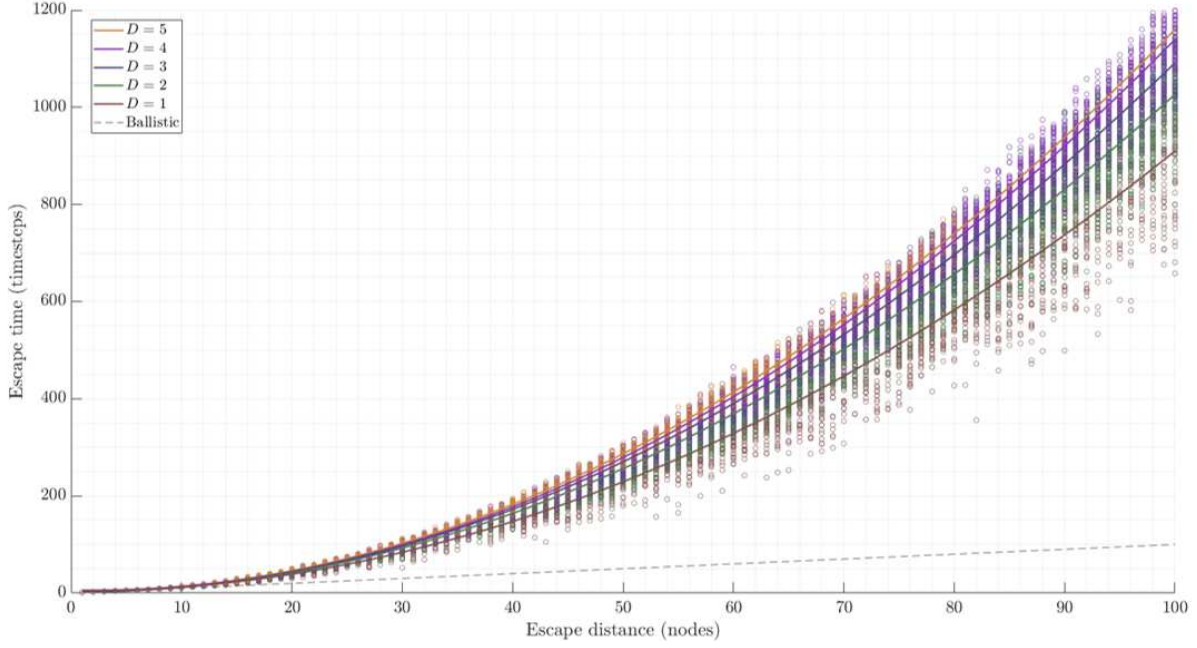
Figure A.9: Representation of escape time trials, $p_1 = \cdots = p_D = \frac{3}{4}$, where walkers start at the centre of a hypercubic lattice where each dimension spans the inclusive interval $[-N, N]$; the escape distance is therefore always N, which is shown on the horizontal axis. A quadratic regression was used to fit the data and each data point represents the fastest escape time of $I = 10^5$ walkers.

(a)

d_i	d_j	$d_i d_j$	$p_d(d_i d_j)$
-1	-1	$+1$	$\frac{p^2}{4}$
0	-1	0	$(1-p)\frac{p}{2}$
$+1$	-1	-1	$\frac{p^2}{4}$
-1	0	0	$(1-p)\frac{p}{2}$
0	0	0	$(1-p)^2$
$+1$	0	0	$(1-p)\frac{p}{2}$
-1	$+1$	-1	$\frac{p^2}{4}$
0	$+1$	0	$(1-p)\frac{p}{2}$
$+1$	$+1$	$+1$	$\frac{p^2}{4}$

(b)

d_i	$p_d(d_i)$	d_j	$p_d(d_j)$	$p_d(d_i d_j)$
-1	$p\delta$	-1	$p\delta$	$p^2\delta^2$
0	$1-p$	-1	$p\delta$	$(1-p)p\delta$
$+1$	$(1-\delta)p$	-1	$p\delta$	$(1-\delta)p^2\delta$
-1	$p\delta$	0	$1-p$	$(1-p)p\delta$
0	$1-p$	0	$1-p$	$(1-p)^2$
$+1$	$(1-\delta)p$	0	$1-p$	$(1-p)(1-\delta)p$
-1	$p\delta$	$+1$	$(1-\delta)p$	$(1-\delta)p^2\delta$
0	$1-p$	$+1$	$(1-\delta)p$	$(1-p)(1-\delta)p$
$+1$	$(1-\delta)p$	$+1$	$(1-\delta)p$	$(1-\delta)^2p^2$

Table A.3: Letting $\langle d_i d_j \rangle = \sum_{\forall i \neq j} d_i d_j p_d(d_i d_j)$ we can see **(a)** the isotropic walk has $\langle d_i d_j \rangle = 0$ due to its symmetry, and **(b)** for the drifting walk, $\langle d_i d_j \rangle = (2\delta - 1)^2 p^2$.
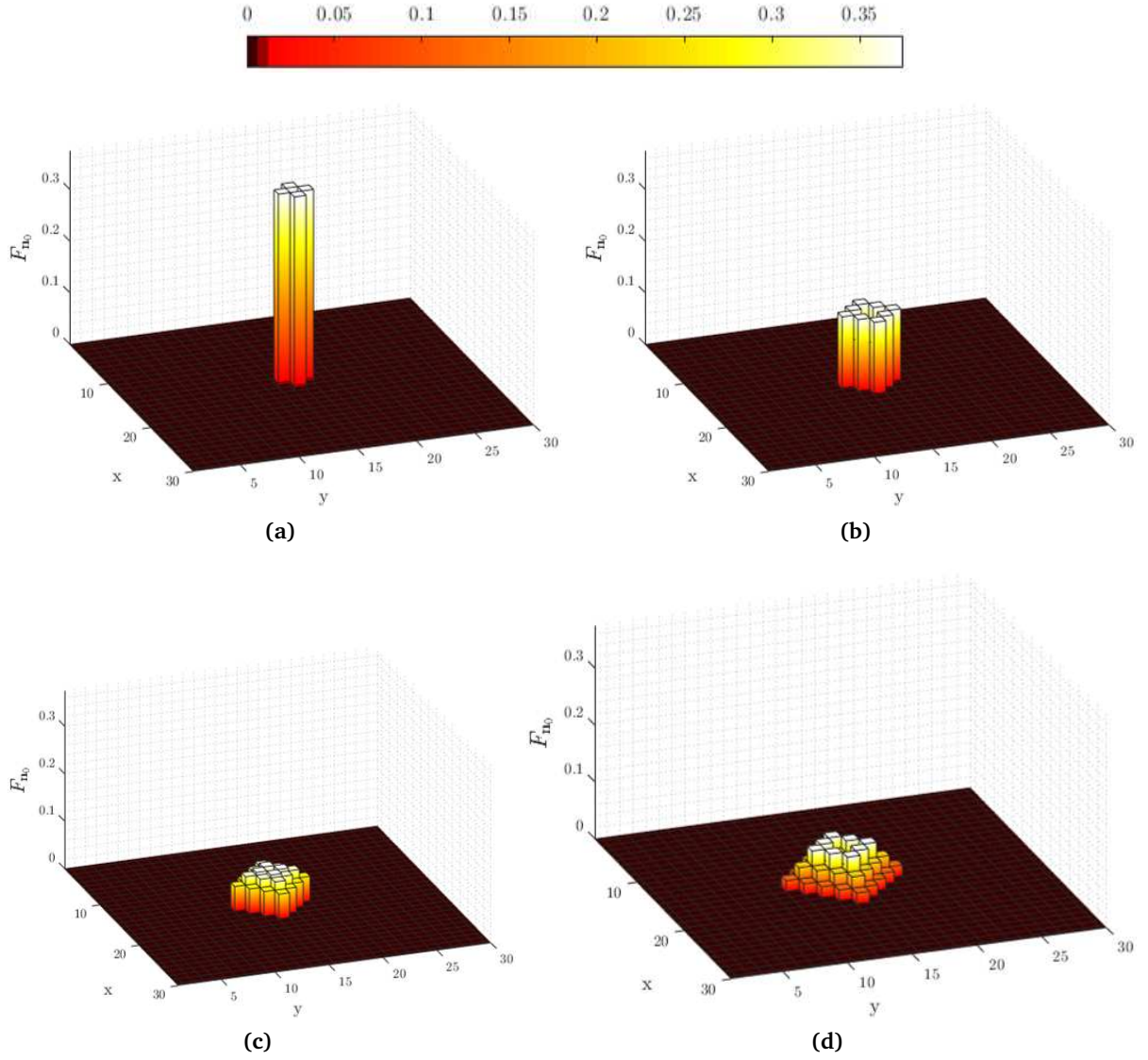
Figure A.10: The first 4 timesteps, in order, of the 2D FPP distribution, on a 30×30 lattice where $p_1 = p_2 = \frac{3}{4}$.

	δ_x	0.5	0.505	0.51	0.52
2D	$\mathrm{E}\left[{}^{(\mathrm{DRF})}t_C\right]$	$154,652.333$	$246,546.670$	$558,275.667$	$5,181,495.176$
	$\mathrm{Std}\left[{}^{(\mathrm{DRF})}t_C\right]$	$43,212.106$	$90,710.008$	$207,317.607$	$1,904,184.310$
3D	$\mathrm{E}\left[{}^{(\mathrm{DRF})}t_C\right]$	$7,080,409.964$	$13,317,288.760$	$33,589,951.800$	
	$\mathrm{Std}\left[{}^{(\mathrm{DRF})}t_C\right]$	$675,184.378$	$1,144,093.384$	$4,040,996.366$	

Table A.4: Numeric ${}^{(\mathrm{DRF})}t_C$ results for various δ_x values for $D = 2, 3$. Trials were performed in a 75×75 lattice where $\delta_z = 0$ where applicable and $\delta_y = 0$ under unanimous $p = \frac{3}{4}$. Evident is the extreme growth of the mean coverage; as such 2D values for $\delta_x > 0.52$ and 3D values for $\delta_x > 0.51$ were too computationally expensive to obtain within reasonable time constraints. Total computation time, for all data in this table, is 86.65 hours split between three simultaneous `MATLAB` instances.
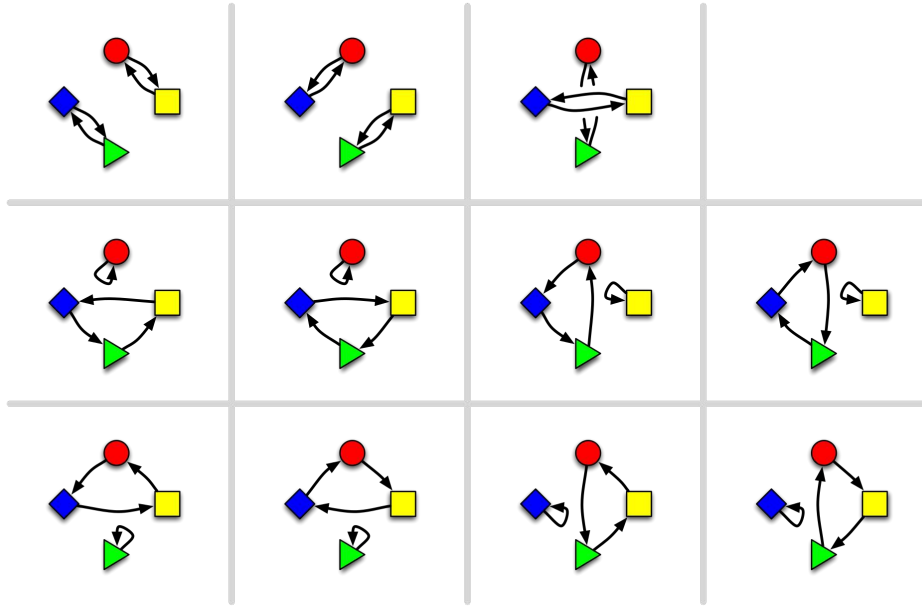
Figure A.11: Combinatoric interpretation of $\left[\begin{smallmatrix}4\\2\end{smallmatrix}\right] = 11$. There are 11 ways to split 4 objects into 2 separate, ordered groups (disjoint cycles). This image was created by Wikipedia user *Stepleton* and shared under the WTFPL.
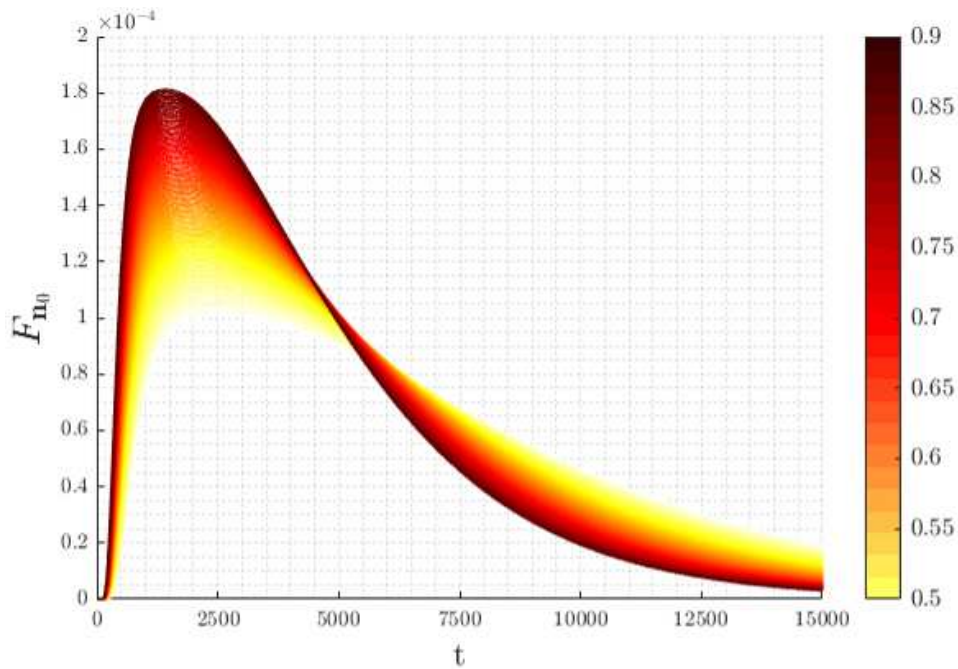

Figure A.12: FPT distribution between $\boldsymbol{n}_0 = [15 \ 15]$ and $\boldsymbol{n} = [30 \ 30]$ on a 30×30 square lattice for different p values, indexed with a colour bar.
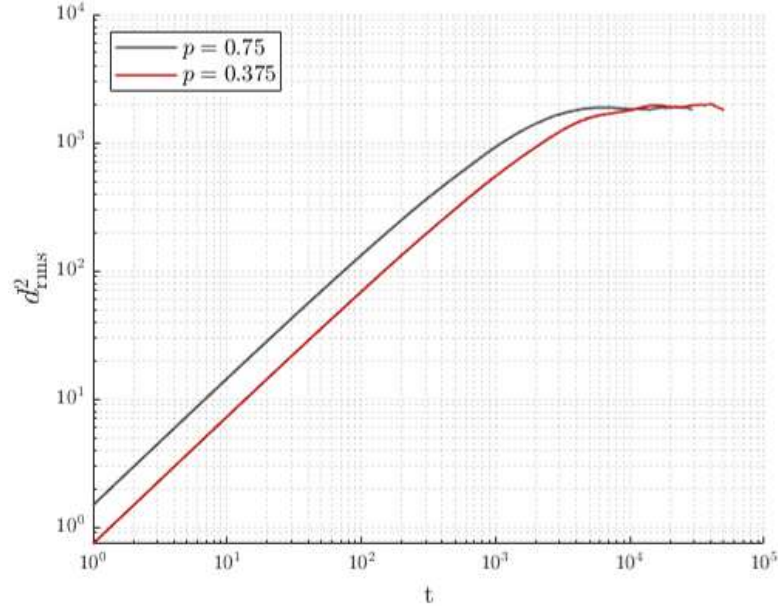
Figure A.13: Log-log MSD plot for $p = \frac{3}{8}, \frac{3}{4}$. As p is multiplicative in $d^2_{\mathrm{rms}}(t) = pt$ its effects in a log-log graph are translational. Hence, doubling p adds $\log 2$ to the $\log y$-intercept; this can be seen here as the intercept rises from 0.7911 to 1.4820. MSD data here was averaged from $I = 300$ RW instances in a 30×30 lattice, with $\boldsymbol{n}_0$ in the centre.
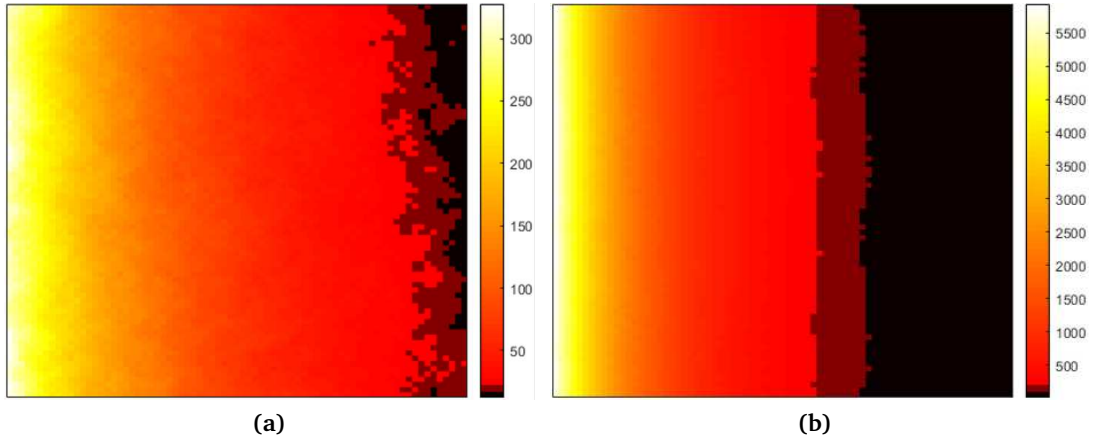

(a)

(b)

Figure A.14: Heatmaps of the same 75×75 lattice as in maintext Figure 4.3 for **(a)** $\delta_x = 0.51$ and **(b)** $\delta_x = 0.52$, also averaged over $I = 300$ walks. Note the increase in the order-of-magnitude of the colour legend. These values are consistent with Appendix Table A.4 – they were calculated from the same simulations.
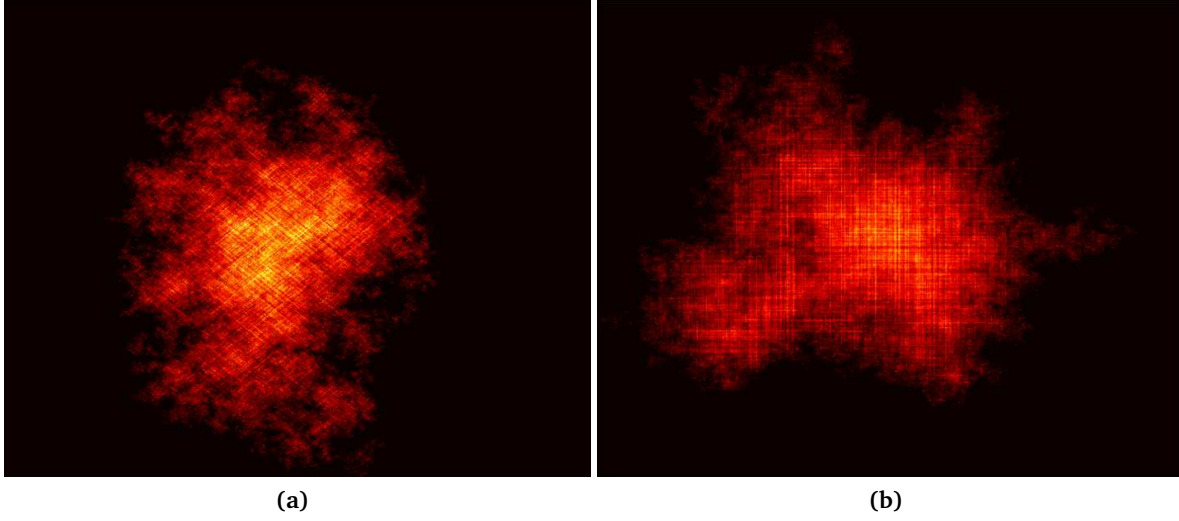
(a)   **(b)**

Figure A.15: Heatmap images of the Muñoz non-Markov walk on first contact with the boundary for **(a)** the NNN walk ($t = 199,356,058$) and **(b)** for the NN case ($t = 703,470,123$). The colouring scale is not shared. Simulations set $p_1 = p_2 = 1$ on a $10,001 \times 10,001$ lattice so as to match the scale in Muñoz et al. [1996].
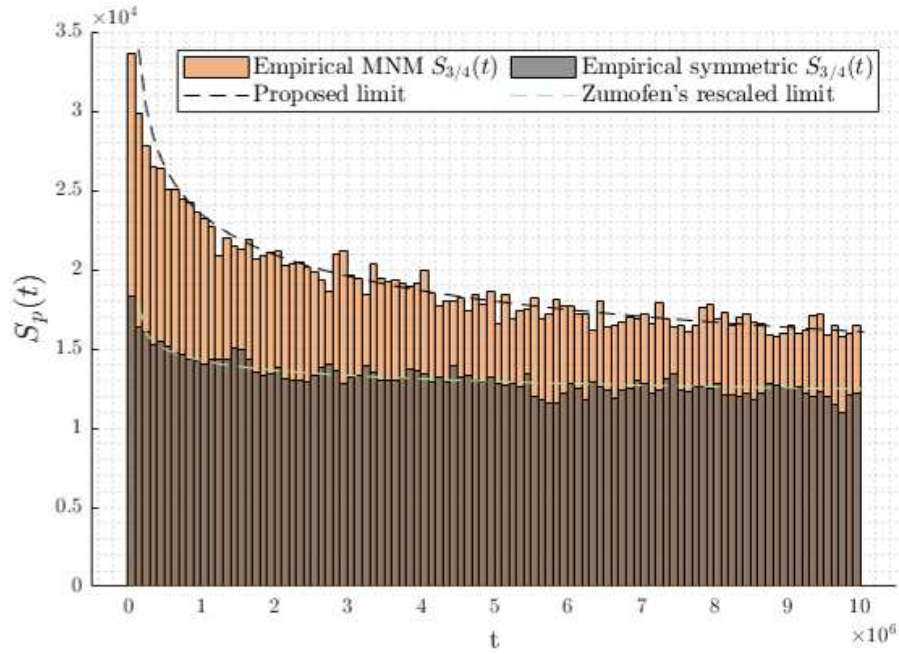

Figure A.16: Comparison of $S_p(t)$ data at $p = \frac{3}{4}$ for symmetric and MNM walks (unconfined). Here Zumofen's limit has been rescaled by p exactly, i.e. we are plotting the approximate derivative of pS_t.
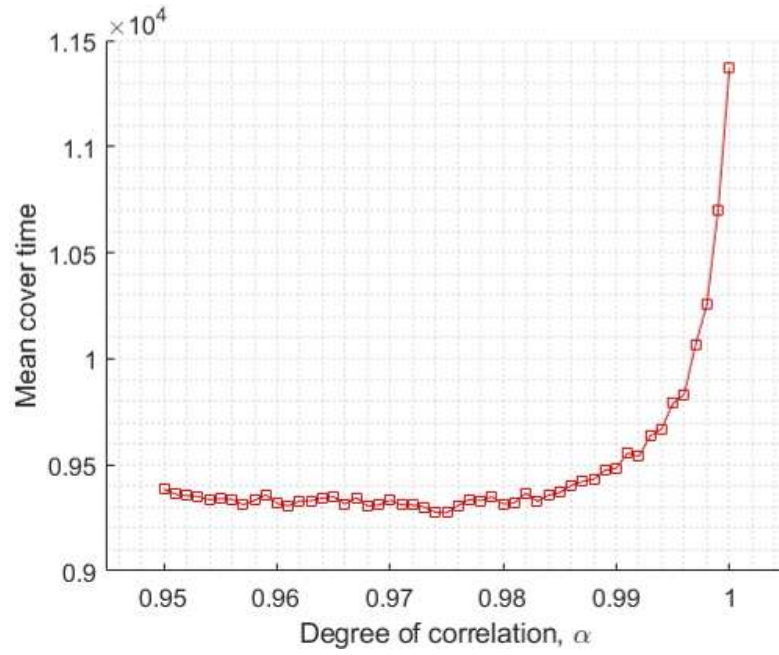
Figure A.17: Using $\Delta\alpha = 0.001$ we show how coverage time is affected by the correlation parameter α on a 75×75 lattice with $p_1 = p_2 = \frac{3}{4}$. Here there is an initial inverse relationship with α, which is carried forward from maintext Figure 4.8a. The range $0.955 \leqslant \alpha \leqslant 0.985$ then remains relatively flat. This is a direct result of both the stochastic variations in RW coverage and of insufficient sampling sizes – this is amended in subsequent simulations in the main text. Finally we observe the effects of parity issues as cover times experience rapid growth for $\alpha > 0.98$. For the aforementioned reasons this run of simulations was also observed to have large standard deviations (average standard deviation 0.7×10^4) hence we omit error bars for clarity. Number of simulations totals $1,470,000$ with total runtime 203 hours using 8 cores of *Blue Crystal phase 3*.
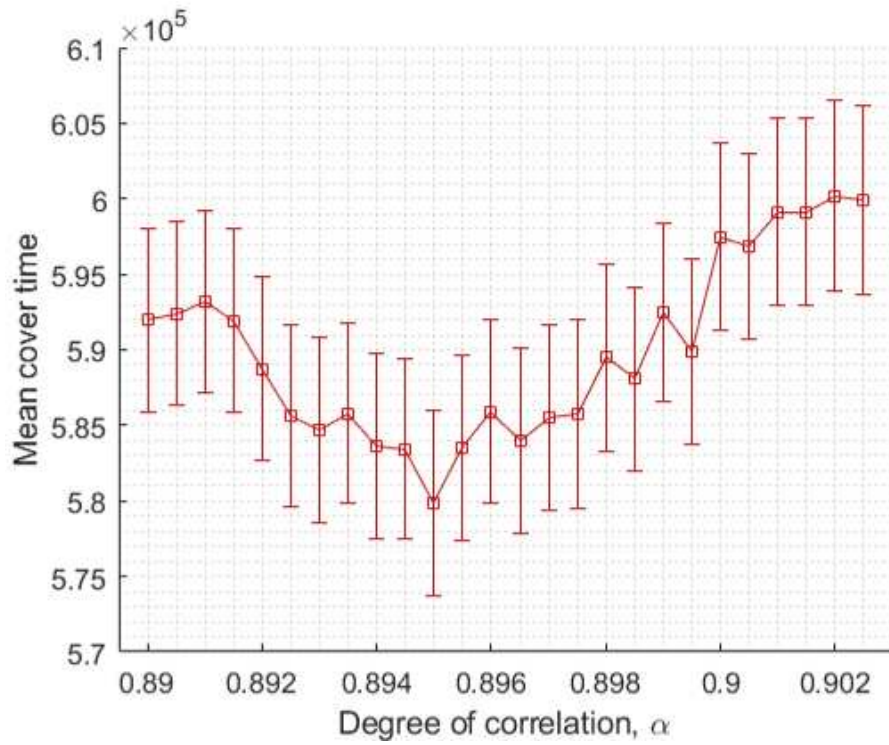
Figure A.18: Mean cover times for increments of $\Delta\alpha = 0.0005$ on a $31 \times 31 \times 31$ cubic lattice with $p = \frac{3}{4}$. The error bars have a length equal to the standard deviation of the samples. Number of simulations total $780,000$, comprised of $30,000$ per data point. This does not show the multiple other simulations which helped find this optimal interval (see Chapter 5). Total runtime here is 164 hours using 16 cores of *Blue Crystal phase 3*.

Given the detailed balance condition

$$\boldsymbol{\pi}_i \boldsymbol{P}_{ij} = \boldsymbol{\pi}_j \boldsymbol{P}_{ji},$$

we can marginalise i to get

$$\sum_{\forall i} \boldsymbol{\pi}_i \boldsymbol{P}_{ij} = \boldsymbol{\pi}_j. \tag{A.1}$$

This is interpreted as the invariance of $\boldsymbol{\pi}$ under the transformation $\boldsymbol{P}$. With specificity to random walks on $\mathbb{Z}$, this says the equilibrium probability at any node j cannot be influenced by executing another timestep. We can now proceed with one of two methods.

For the first method we note that $\boldsymbol{P}$ is tridiagonal; $\boldsymbol{P}_{ij} \neq 0$ if and only if $j - 1 \leqslant i \leqslant j + 1$. Also, let $\boldsymbol{\pi} = [\pi_1 \ \pi_2 \ \cdots \ \pi_N]$. Equipped with this, we can substitute values into (A.1) and show it is synonymous with the following system of N linear equations:

$$(1 - \frac{p}{2})\pi_1 \ + \ \frac{p}{2}\pi_2 \ = \ \pi_1, \tag{A.2a}$$

$$\frac{p}{2}\pi_1 \ + \ (1-p)\pi_2 \ + \ \frac{p}{2}\pi_3 \ = \ \pi_2, \tag{A.2b}$$

$$\frac{p}{2}\pi_2 \ + \ (1-p)\pi_3 \ + \ \frac{p}{2}\pi_4 \ = \ \pi_3, \tag{A.2c}$$

$$\vdots$$

$$\frac{p}{2}\pi_{N-3} \ + \ (1-p)\pi_{N-2} \ + \ \frac{p}{2}\pi_{N-1} \ = \ \pi_{N-2}, \tag{A.2d}$$

$$\frac{p}{2}\pi_{N-2} \ + \ (1-p)\pi_{N-1} \ + \ \frac{p}{2}\pi_N \ = \ \pi_{N-1}, \tag{A.2e}$$

$$\frac{p}{2}\pi_{N-1} \ + \ (1 - \frac{p}{2})\pi_N \ = \ \pi_N. \tag{A.2f}$$

The expressions for π_1 and π_N can then be solved immediately:

$$\pi_1 = \pi_2,$$

$$\pi_N = \pi_{N-1}.$$

Solving the bulk of the equations follows suit; substituting $\pi_1 = \pi_2$ into (A.2b) gives $\pi_2 = \pi_3$; substituting that into (A.2c) gives $\pi_3 = \pi_4$; substituting that into the next will give $\pi_4 = \pi_5$, and so on. We remind ourselves that the detailed balance condition assumes a unit π vector, and so finally we write

$$\boldsymbol{\pi} = \begin{bmatrix} \frac{1}{N} & \frac{1}{N} & \cdots & \frac{1}{N} \end{bmatrix},$$

which can be shown to be the correct equilibrium occupational probability – intuitively, analytically, or through simulations – and confirms the assumption of time reversibility.

The alternative method realises that (A.1) is just the index form of

$$\boldsymbol{\pi P} = \boldsymbol{\pi}, \tag{A.3}$$

since $j = 1, 2, \ldots, N$ and $\boldsymbol{\pi} \in \mathbb{R}^N$. This method then realises that (A.3) is a special case of the eigenvector equation, stating that $\boldsymbol{\pi}$ is the eigenvector of $\boldsymbol{P}$ corresponding to the unit eigenvalue. This agrees with the interpretation given under Equation (A.1). Maintaining our notation from Chapter 2, we write $\lambda_k = 1$; recalling Equation (2.3) we see this is true only when $k = 1$, irrespective of N, p. Bearing in mind the occupational probability function P_{n_0} is comprised of a sum of N quantities closely linked to each of the N eigenvalues, we reason that extracting only the $k = 1$ summands corresponds to the probability induced only by the $\lambda_{k=1} = 1$ eigenvalue from (A.3). Moreover, the $k = 1$ summands are all unity, and thus support the invariance to n, t we know the equilibrium distribution to have. This allows us to equate the $k = 1$ summands to the probabilities at equilibrium. Again, the detailed balance condition assumes a unit $\boldsymbol{\pi}$ vector, meaning

$$\boldsymbol{\pi} = \begin{bmatrix} \frac{1}{N} & \frac{1}{N} & \cdots & \frac{1}{N} \end{bmatrix},$$

after which we arrive at the same conclusions as above and in Chapter 3.